Interaction between edge dislocations and amorphous interphase in carbon nanotubes reinforced metal matrix nanocomposites incorporating interface effect

Shuhong Dong [a], Jianqiu Zhou [a,b,∗], David Hui [c], Xuming Pang [a], Qian Wang [a], Shu Zhang [a], Lu Wang [a]

[a] Department of Mechanical Engineering, Nanjing University of Technology, Nanjing, Jiangsu Province, 210009, China
[b] Department of Mechanical Engineering, Wuhan Institute of Technology, Wuhan, Hubei Province 430070, China
[c] Department of Mechanical Engineering, University of New Orleans, New Orleans, LA 70148, United States

ABSTRACT

Dislocations mobility and stability in the carbon nanotubes (CNTs)-reinforced metal matrix nanocomposites (MMNCs) can significantly affect the mechanical properties of the composites. However, current processing techniques often lead to the formation of coated CNT (amorphous interphase exists between the reinforcement and metal matrix), which have large impact upon the image force exerting on dislocations. Even though the importance of the interphase zone formed in metal matrix composites has been demonstrated by many studies for elastic properties, the influence of interphase on the local elastoplastic behavior of CNT-reinforced MMNCs is still an open issue. This paper puts forward a three-phase composite cylinder model with new boundary conditions. In this model, the interaction between edge dislocations and a coated CNT incorporating interface effect is investigated. The explicit expressions for the stress fields and the image force acting on an edge dislocation are proposed. In addition, plastic flow occurring around the coated reinforcement is addressed. The influences of interface condition and the material properties of coated CNT on the glide/climb force are clearly analyzed. The results indicate that the interface effect becomes remarkable when the radius of the coated reinforcement is below 10 nm. In addition, different from the traditional particles, the coated CNT attracts the adjacent edge dislocations, causing pronounced local hardening at the interface between the interphase and the metal matrix under certain conditions. It is concluded that the presence of the interphase can have a profound effect on the local stress field in CNT-reinforced MMNCs. Finally, the condition of the dislocations stability and the equilibrium numbers of dislocations at a given size grain are evaluated for considering the interface effect.

© 2013 Elsevier Ltd. All rights reserved.

1. Introduction

Carbon nanotubes (CNTs) have attracted tremendous expectation as reinforcements to improve the mechanical performance of monolithic materials due to their extraordinary mechanical properties as compared with pure metal (Treacy et al., 1996). Numerous research studies have been undertaken on synthesis and characterization of CNT/metal matrix composites since the first article appeared in 1998 on CNT/Al composite (Kuzumaki et al., 1998). Recently, Bakshi et al. (2010) have presented a review summarizing the research work carried out in the field of carbon nanotubes reinforced metal matrix nanocomposites (MMNCs), which elucidated the influence of CNT volume concentration, dispersion, strengthening mechanisms, and CNT-matrix interfacial conditions on the overall elastic and plastic behavior of the composites.

However, compared with CNT-reinforced polymer matrix composites (PMCs) (Fisher et al., 2003; Odegard et al., 2003; Odegard et al., 2004; Coleman et al., 2006; Namilae and Chandra, 2006; Wang et al., 2008; Jia et al., 2011; Tehrani et al., 2011) and ceramic matrix composites (CMCs) (Flahaut et al., 2000; Rul et al., 2004; Xia et al., 2004; Yamamoto et al., 2008; Ahmad et al., 2010; Liu et al., 2011a), studies on MMNCs reinforced by CNT are comparatively fewer, and the improvement of the mechanical properties of bulk CNT/metal matrix composites is not commensurate with the expectation. This is mainly because of difficulties in uniformly distributing CNT in most metallic matrices and weak interfacial issues between the reinforcements and matrices. Agglomeration of CNT could lead to premature failure of the composites, and various processing techniques have been adopted to avoid such a highly undesirable condition. In addition, the interfaces between CNT

∗ Corresponding author at: Department of Mechanical Engineering, Nanjing University of Technology, Nanjing, Jiangsu Province 210009, China. Tel.: +86 25 83588706; fax: +86 25 83374190.

E-mail address: zhouj@njut.edu.cn (J. Zhou).

and metal matrix are also critical to the pursuit of enhanced mechanical properties of the composites, even when CNT are uniformly dispersed. The most possible phenomenon may be the formation of nanosize carbides on the interfaces between CNT and matrix and this may affect the load transfer condition between them (Ci et al., 2006; Deng et al., 2007; Esawi et al., 2010). These particles are likely to be the by-products of chemical reactions between the metal powders and amorphous carbon atoms around pristine CNT and found to be closely attached to the surfaces of the reinforcement. Moreover, Kim et al. (2008) have observed many oxygen-rich regions existing near the CNT or on their surfaces. The good agreement of yield strength and elastic modulus between the measured values and the ones calculated by both the shear-lag and the Eshelby model, demonstrating that oxygen atoms presenting at the CNT/Cu interface play a significant role in accommodating the load transfer between matrix and reinforcement. Besides, the amorphous interphase was revealed to form around CNT in CNT/Cu composites after hydrogen reduction and consolidation (Cho et al., 2012), which was composed of amorphous carbon atoms and oxygen atoms. Similarly, Balani and Agarwal (2008) also observed that the molten metal spread uniformly on the surfaces of CNT and formed thin layers (about 20–25 nm) without any cracks. In fiber-reinforced composites, coatings on fibers are widely employed to improve the bonding conditions between fibers and matrix (Hashin, 2002; Gao et al., 2008). A coating layer can control the delamination of the interface and inhibit cracks initiated external to the reinforcement from damaging the matrix. Recently, Yang et al. (2013) have proposed a nonlinear multiscale modeling approach to characterize the elastoplastic behavior of CNT-reinforced PMCs with considering the interphase. The study focused on the identification of local elastic and plastic behavior of the interphase region from the well known elastoplastic properties of the nanocomposites. In a word, the presence of interphase around CNT in CNT-reinforced MMNCs can significantly affect the local stress field distribution and greatly change the load transfer conditions between reinforcement and matrix. Even though the importance of the interphase zone has been demonstrated by many investigations for elastic properties (Shen and Li, 2003; Mogilevskaya and Crouch, 2004; Mogilevskaya et al., 2010), studies on the influence of interphase on the local elastoplastic behavior of CNT-reinforced MMNCs is still an open issue. We expected to look into the issue in this paper.

Up until now, three strengthening mechanisms have been developed to predict the yield strength of CNT-reinforced MMNCs, two among them, namely Orowan strengthening and thermal mismatch, containing the dislocation effect (George et al., 2005; Li et al., 2009). Dislocations are the carriers of plasticity in crystalline materials and their mobility and stability around inclusions in the matrix can affect the mechanical behaviors of composites. CNT-reinforced MMNCs are often prepared under severe conditions, such as high temperature and high pressure (Xu et al., 1999; Kwon et al., 2009). Residual stresses will build up during the cooling process due to the significant coefficient of thermal expansion (CTE) and the elastic-plastic properties mismatch between CNT and matrix. The stresses around the reinforcement are large enough to cause plastic deformation in the matrix, especially in the interface region, and then generate small defects such as a high density of dislocations in the vicinity of nanosized particles (Hiratani et al., 2003; Aghababaei and Joshi, 2013). Ashby (1966) proposed that the stress concentration around a particle in a second-phase particle/matrix system was relieved by the nucleation and movement of prismatic loops along a secondary slip system. When the magnitude of the local resolved shear stress exceeds a certain value, dislocation loops (the pairs of opposite-signed edge dislocations) will be nucleated at random sites along the slip planes and punched out into the matrix (Taya et al., 1991; Shibata et al., 1992; Lubarda, 2011). The

ductility improvement of CNT/Mg composites was observed to be the result of the initiation of prismatic slip and the activation of the basal slip system, and one of the main hardening reasons of the composites was identified to be the formation of sessile forest dislocations (Goh et al., 2008). These studies have shed significant insights into the generation and movement of dislocations in CNT-reinforced MMNCs, but none has touched upon the interaction between dislocations and amorphous interphases encircled CNT. The interactions between dislocations and nearby second phase or misfit stress field are of great importance, which can modify the overall yield behavior of the composites (Qaissaunee and Santare, 1995; Hu et al., 2004; Khraishi et al., 2004; Wang et al., 2010). In view of this importance, the problem has received much attention in the last decades, and is often simulated by employing the three-phase composite cylinder model (Dundurs and Mura, 1964; Luo and Chen, 1991; Ru, 1999; Xiao and Chen, 2001; Sudak et al., 2002; Wang and Shen, 2002; Fang et al., 2009a; Wang and Pan, 2011). In addition, it is well known that in the classical dislocations-particles analysis, dislocations are repelled from second phase when the shear moduli of the inclusions are higher than those of the matrices. However, when interface bonding is modified by imperfect interface boundary conditions or diffusional relaxations, these interactions may be completely reverse (Gao, 1992).

In recent years, to deeply address the size-dependent elastic and plastic fields created by nanoscale inclusions, the surface/interface stress model has been extensively developed on account of the rapid development of nanotechnology (Fang and Liu, 2006; Lim et al., 2006; Zhang et al., 2010; Bakhshayesh et al., 2012; Gutkin et al., 2013). Jiang et al. (2006) has developed a cohesive law for CNT/polymer interfaces to estimate the surface effect by employing the atomistic model. Since atoms near and between the interfaces have different energies from those in the interior of the inclusions or matrix, surface/interface stress appears. In general, when the matrix with large grain size, the volume ratio of the interface region to the bulk material is small, the effect of the interface stress is insignificant. However, for fine-scaled materials, especially for nanocrystalline composites, with a large ratio of the interface region to the matrix, the interface plays a very important role in affecting the elastic-plastic deformation behaviors of the composites (Yassar et al., 2007). A lot of theories (Liu et al., 2009; Liu et al., 2010) give us some hints that the difference of the plastic deformation behavior between nanostructured materials and coarse-grained materials is essentially size-dependent. In the present study, we pay close attention to the impact of interface stress upon the mobility and stability of dislocations.

In addition to the role of interphase and interface, it is also important to consider the influence of the matrix grain size on the stresses experienced by dislocations and their stability. Compared with the coarse grains, the activity of conventional dislocation sources is inhibited in nanoscale grains. In that situation, amorphous intergranular boundaries (AIBs) are expected to become the sources for lattice dislocation nucleation in deformed nanocomposites (Bobylev et al., 2009). In addition, atomic simulations Wang et al. (2007) demonstrated that the amorphous crystalline interfaces (ACIs) exhibited unique inelastic shear transfer characteristics, different from those of grain boundaries (GBs). Dislocations can be emitted from ACIs or from GBs or ACIs-GBs intersections and absorbed at the opposite ACIs. However, if grain size is relatively small (of the order of nanometers), the dislocations emitted from ACIs usually are retarded at the opposite GBs and impede further dislocations emission, the ductility is often reduced dramatically. As a result, the addition of nanoscale amorphous layers may offer great benefits in constructing the plasticity of crystalline composites, and opening new approaches for improving their strength and ductility. However, the micromechanism of dislocations emitted from the interface between interphase and matrix is unclear. Such a

micromechanism is of significance for understanding the essentials of plastic flow and its transfer from amorphous interphase to nearest crystalline in MMNCs (Bobylev et al., 2009).

To address the effect of amorphous interphase on the plastic flow occurring around the reinforcement and the interaction between edge dislocations and a coated mutli-walled carbon nanotube (MWCNT) with interface effect, a three-phase composite cylinder model combined with new boundary conditions is developed in Section 2. By means of the typical analytical continuation technique of complex potentials, the stress fields within the matrix, the amorphous interphase and MWCNT are also derived in this Section. The plastic flow occurring around the reinforcement and the emission of dislocations from amorphous interphase are addressed in Section 3. In addition, a two-phase composite model is also introduced for comparison. In Section 4, based on the stress distribution in the matrix, the image force acting on dislocations is discussed in detail. Then the stability of edge dislocations at a given size grain and equilibrium numbers of dislocations are evaluated in terms of the total force balance equations in this section. These formulations automatically include the effect of the size (radius) and elastic constants of MWCNT, amorphous interphase and interface effect. In this way, the influences of MWCNT, amorphous interphase and interface conditions on edge dislocations can all be assessed, and compared with some available experimental results, theories and computer simulations to validate the applicability of the proposed three-phase composite cylinder model. Finally, Section 5 provides a summary and a discussion of some extensions of this paper.

2. Description on the model of amorphous interphase in CNT-reinforced composite

2.1. Morphology of the CNT-reinforced MMNCs

A typical schematic of the interaction between a coated MWCNT and an edge dislocation in an infinite elastic plane subjected to remote biaxial loading is presented (see Fig. 1). We consider a solitary MWCNT with an outer radius R_1 bonded to an infinite elastic matrix through a coaxial circular interphase in a
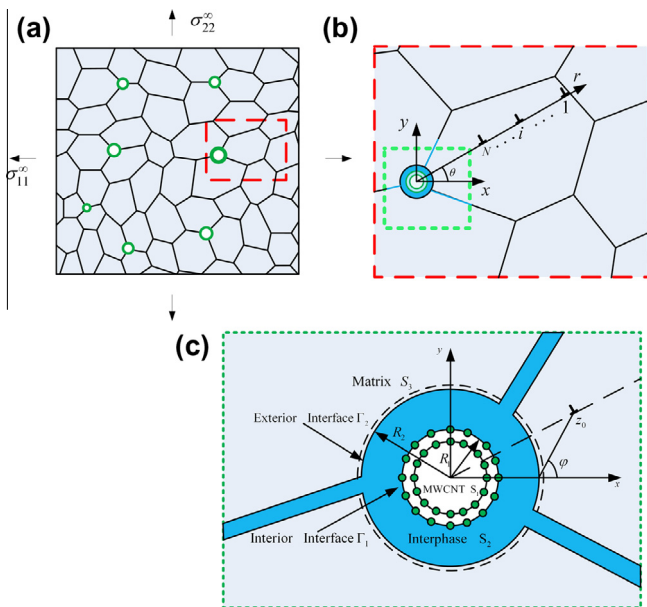

Fig. 1. A solitary coated MWCNT in deformed nanocomposites subjected to remote biaxial loading: (a) General view of CNT-reinforced MMNCs; (b) The magnified inset emphasizes the emission of dislocations from the interface between amorphous interphase and matrix; (c) An edge dislocation near the coated MWCNT in the three-phase cylinder composite model.

triple junction. The thickness of the coating phase is $R_2 - R_1$. Let S_1, S_2 and S_3 denote the MWCNT, the interphase and the surrounding matrix, respectively. Without loss of generality, the subscripts 1, 2 and 3 are adopted to identify the respective holomorphic function in the region S_1, S_2 and S_3. In addition, an edge dislocation with Burger's vector $B = b_x + ib_y$ is assumed to be located at an arbitrary point z_0 in the matrix S_3, and the three-phase composite system model is subjected to remote uniform loadings σ_{11}^∞ and σ_{22}^∞.

2.2. Basic formula and problem statement

The hexagonal distribution of carbon atoms and the hollow nature of the tube make the overall elastic properties of CNT transversely isotropic (Shen and Li, 2004, 2005; Barai and Weng, 2011). CNT will be considered to only deform elastically in this paper. In order to deal with the transversely isotropic elastic response, it is convenient to adopt Hill's stress-strain relations (Hill, 1964). So the explicit form can be written in the polar coordinates

$$(\sigma_{rr} + \sigma_{\theta\theta}) = 2k(\varepsilon_{rr} + \varepsilon_{\theta\theta}) + 2l\varepsilon_{zz}, \tag{1}$$

$$\sigma_{zz} = l(\varepsilon_{rr} + \varepsilon_{\theta\theta}) + q\varepsilon_{zz}, \tag{2}$$

$$(\sigma_{\theta\theta} - \sigma_{rr}) = 2m(\varepsilon_{\theta\theta} - \varepsilon_{rr}), \tag{3}$$

$$\sigma_{r\theta} = 2m\varepsilon_{r\theta}, \sigma_{\theta z} = 2p\varepsilon_{\theta z}, \sigma_{rz} = 2p\varepsilon_{rz}. \tag{4}$$

where k, l, q, m and p are the plane-strain bulk modulus for lateral dilatation, associated cross modulus, axial modulus for longitudinal uniaxial strain, the transverse shear modulus and axial shear modulus, respectively. Then, in Walpole's scheme (Walpole, 1969; Walpole, 1981), due to its diagonally symmetric and positive definite, the tensor of transversely isotropic elastic modulus L can be expressed as

$$L = (2k, l, q, 2m, 2p). \tag{5}$$

In terms of the traditional engineering constants, L is equivalent to

$$L = (2\kappa_{r\theta}, C_{rz}, C_{zz}, 2\mu_{r\theta}, 2\mu_{rz}). \tag{6}$$

with direction z as the axial direction and plane $r - \theta$ isotropic, the major Poisson ratio and longitudinal Young's modulus are given by $v_{rz} = l/2k$ and $E_{zz} = q - l^2/k$.

For the interaction of edge dislocations with coated CNT, the interface boundary conditions are important factors that affect the stress fields and image forces acting on the dislocations. Although the amorphous interphase has a tight contact with CNT, the interphase is imperfectly bonded to matrix along the curve Γ_2 due to the big difference of the surface tensions between the two materials (Nuriel et al., 2005; So et al., 2011). The interphase can assumed to be perfectly adhered to the MWCNT without slipping along the curve Γ_1, while only displacement is continuous across the imperfect interface Γ_2. In view of this, according to the theory proposed by Gurtin and Murdoch (1975) and Sharma et al. (2003), for an isotropic elastic plane in the absence of body force, the following elastic field equations and constitutive relations for interface Γ_1 can be established respectively.

$$[[\sigma_{rr} - i\sigma_{r\theta}]] = 0, \quad [[u_r + iu_\theta]] = 0, \quad z \in \Gamma_1, \tag{7}$$

And the interface condition along Γ_2 can be written in the form

$$[[\sigma_{rr} - i\sigma_{r\theta}]] = \frac{\sigma_{\theta\theta}^0}{R_2} + i\frac{1}{R_2}\frac{\partial \sigma_{\theta\theta}^0}{\partial \theta}, \quad [[u_r + iu_\theta]] = 0, \quad z \in \Gamma_2. \tag{8}$$

where the brackets $[[*]] = (*)_2 - (*)_1$ or $(*)_3 - (*)_2$ denote the jump of the said quantity across $\Gamma_k(k = 1, 2)$, respectively. The superscript 0 represents the interface region, and $z \in \Gamma_k$ $(k = 1, 2)$ denotes the points on the circular arc surfaces $\Gamma_k(k = 1, 2)$.

In addition, the interface region Γ_2 can be characterized by an additional constitutive equation (Tian and Rajapakse, 2007)

$$\sigma_{\theta\theta}^0 = \tau^0 + 2(\mu^0 - \tau^0)\varepsilon_{\theta\theta}^0 + (\lambda^0 + \tau^0)(\varepsilon_{\theta\theta}^0 + \varepsilon_{zz}^0). \tag{9}$$

where λ^0 and μ^0 are the interface elastic constants, τ^0 is the residual interface stress. It is well known that the interfaces between different phases can be incoherent, semi-coherent or coherent (Romanov et al., 1998; Zbib et al., 2011). Coherent interfaces are commonly presented within materials under a wide range of conditions (Duan et al., 2005), and to the extent when an interface is coherent, the interfacial strain $\varepsilon_{\theta\theta}^0 = \varepsilon_{\theta\theta 2}$, $\varepsilon_{zz}^0 = \varepsilon_{zz2}$, where $\varepsilon_{\theta\theta 2}$ is the associated tangential strain in the adjacent bulk materials, i.e., amorphous interphase. As mentioned above, the amorphous interphase is closely attached to the surface of MWCNT and its tangential strain can be supposed to equal to the elastic strain $\varepsilon_{\theta\theta 1}$ and ε_{zz1} of MWCNT. Here we restrict our attention to coherent interfaces and take interface Γ_2 as a coherent one.

In what follows, our study is confined to the plane deformation of transversely isotropic elastic materials. The problem of an infinite elastic plane containing a coated circular inclusion is usually analyzed by employing the classical complex potential method (Muskhelishvili, 1953). For a region bounded by a circle of radius R, its stress components and displacement fields can be expressed by two complex potentials $g(z)$ and $h(z)$

$$2\mu(u_x' + iu_y') = iz\left[\kappa g(z) + g\left(\frac{R^2}{\bar{z}}\right) - \bar{z}\left(\frac{\bar{z}}{R^2} - \frac{1}{z}\right)\overline{h(z)}\right], \tag{10}$$

$$\sigma_{rr} + \sigma_{\theta\theta} = 2[g(z) + \overline{g(z)}], \tag{11}$$

$$\sigma_{rr} + i\sigma_{r\theta} = g(z) - g\left(\frac{R^2}{\bar{z}}\right) + \bar{z}\left(\frac{\bar{z}}{R^2} - \frac{1}{z}\right)\overline{h(z)}. \tag{12}$$

where $z = x + iy = re^{i\theta}$ is the complex variable, $u_x' = \partial u_x/\partial\theta$, $u_y' = \partial u_y/\partial\theta$. For the plane deformation of isotropic materials, $\kappa = 3 - 4\nu$, while $\kappa = 1 + 2\mu_{rz}/K_{r\theta}$ for the plane deformation problem of transversely isotropic materials; and μ_{rz} and $K_{r\theta}$ are the in-plane shear modulus and the plane-strain bulk modulus of transversely isotropic materials; μ and ν are the in-plane shear modulus and the Poisson's ratio, respectively. In addition, in order to deal with the boundary conditions on the interfaces, the analytical continuation is introduced and defined as (Luo and Chen, 1991)

$$h(z) = \frac{R^2}{z^2}\left[g(z) + \bar{g}\left(\frac{R^2}{z}\right) - zg'(z)\right]. \tag{13}$$

Since CNT have large aspect ratio, we suppose that the tube walls of CNT bear most of loads under the given condition, rather than playing the role of bridging on the cracks in MMCs. So debonding can be assumed to occur at the ends of the reinforcements. Considering the constitutive relations (1)-(4) for CNT, one can obtain the expressions of the elastic strain $\varepsilon_{\theta\theta 1}$ and ε_{zz1} in terms of $\sigma_{33} = 0$

$$\varepsilon_{\theta\theta 1} = \left(\frac{q}{4kq - 4l^2} - \frac{1}{4m}\right)\sigma_{rr1} + \left(\frac{q}{4kq - 4l^2} + \frac{1}{4m}\right)\sigma_{\theta\theta 1}, \tag{14}$$

$$\varepsilon_{\theta\theta 1} + \varepsilon_{zz1} = \left(1 - \frac{2l}{q}\right)\varepsilon_{\theta\theta 1} + \frac{l}{2mq}(\sigma_{\theta\theta 1} - \sigma_{rr1}). \tag{15}$$

To derive the stress fields around coated MWCNT, the mission now is simplified to determine the complex analytical functions $g_1(z)$, $h_1(z)$, $g_2(z)$, $h_2(z)$, $g_3(z)$ and $h_3(z)$ within the region $R < R_1$ (the MWCNT), region $R_1 < R < R_2$ (the nanoscale interphase) and region $R > R_2$ (the matrix) under the boundary conditions, respectively.

2.3. Stress fields of three-phase composite model with amorphous interphase

2.3.1. The boundary conditions on the interior interface Γ_1

According to Eqs. (11) and (12), the continuity conditions of traction and displacement across the interface Γ_1, i.e., Eq. (7) can be expressed into a useful form

$$[g_1(t) + g_2(t)]^+ = [g_1(t) + g_2(t)]^-, \tag{16}$$

$$\frac{1}{2\mu_1}[\kappa_1 g_1^+(t) + g_1^-(t)] = \frac{1}{2\mu_2}[\kappa_2 g_2^-(t) + g_2^+(t)], \quad |t| = R_1. \tag{17}$$

where the superscripts "+" and "−" represent the values obtained as z approaches to the interface from the inner Γ_k^+ or outer side Γ_k^- ($k = 1, 2$) of the contour, respectively.

According to the given boundary conditions, the expressions of complex analytical functions $h_1(z)$ within the MWCNT and $h_2(z)$ in the nanoscale interphase are obtained as follow (the detailed calculations are listed in Appendix A.)

$$h_1(z) = \frac{R_1^2}{z^2}\left[\frac{\beta}{\alpha}\sum_{n=1}^{+\infty}\overline{A_{-n}}\left(\frac{z}{R_1^2}\right)^n - \beta\sum_{n=1}^{+\infty}A_n(n-1)z^n\right], \quad |z| < R_1, \tag{18}$$

$$\begin{aligned}h_2(z) = \frac{R_1^2}{z^2}&\left[\frac{1-\alpha}{1-\alpha+\beta}(A_0 + \overline{A_0}) - \sum_{n=1}^{+\infty}A_n(n-1)z^n + \sum_{n=1}^{+\infty}\overline{A_{-n}}\left(\frac{z}{R_1^2}\right)^n\right.\\&\left.+(1-\beta)\sum_{n=1}^{+\infty}\overline{A_n}\left(\frac{R_1^2}{z}\right)^n + \left(1 - \frac{\beta}{\alpha}\right)\sum_{n=1}^{+\infty}A_{-n}(n-1)z^{-n}\right],\\&R_1 < |z| < R_2.\end{aligned} \tag{19}$$

2.3.2. The boundary conditions on the exterior interface Γ_2

The stress discontinuity conditions at the interface Γ_2 in Eq. (8) can be written with the aid of Eq. (9) as

$$\sigma_{rr2}^+(z) - \sigma_{rr3}^-(z) = -\frac{\tau^0}{R_2} - \frac{2(\mu^0 - \tau^0)}{R_2}\varepsilon_{\theta\theta 2} - \frac{\lambda^0 + \tau^0}{R_2}(\varepsilon_{\theta\theta 2} + \varepsilon_{zz2}), \tag{20}$$

$$\sigma_{r\theta 2}^+(z) - \sigma_{r\theta 3}^-(z) = \frac{1}{R_2}\frac{\partial\tau^0}{\partial\theta} + \frac{2(\mu^0 - \tau^0)}{R_2}\frac{\partial\varepsilon_{\theta\theta 2}}{\partial\theta} + \frac{\lambda^0 + \tau^0}{R_2}\frac{\partial(\varepsilon_{\theta\theta 2} + \varepsilon_{zz2})}{\partial\theta}, \tag{21}$$

It is convenient to rewrite the above equations as follows

$$\begin{aligned}[\sigma_{rr2} + i\sigma_{r\theta 2}]^+ - [\sigma_{rr3} + i\sigma_{r\theta 3}]^- &= [\sigma_{rr2}^+ - \sigma_{rr3}^-] + i[\sigma_{r\theta 2}^+ - \sigma_{r\theta 3}^-]\\&= -\frac{\tau^0}{R_2} - \frac{2(\mu^0 - \tau^0)}{R_2}\varepsilon_{\theta\theta 2}\\&\quad - \frac{\lambda^0 + \tau^0}{R_2}(\varepsilon_{\theta\theta 2} + \varepsilon_{zz2}) + i\frac{1}{R_2}\\&\quad\times\frac{\partial\tau^0}{\partial\theta} + i\frac{2(\mu^0 - \tau^0)}{R_2}\frac{\partial\varepsilon_{\theta\theta 2}}{\partial\theta}\\&\quad + i\frac{\lambda^0 + \tau^0}{R_2}\frac{\partial(\varepsilon_{\theta\theta 2} + \varepsilon_{zz2})}{\partial\theta},\end{aligned} \tag{22}$$

From Eqs. (11) and (12), it is found that

$$\sigma_{\theta\theta 2} + \sigma_{rr2} = 2[g_2(z) + \overline{g_2(z)}], \tag{23}$$

$$\begin{aligned}\sigma_{\theta\theta 2} - \sigma_{rr2} = g_2(z) + \overline{g_2(z)} + g_2\left(\frac{R_2^2}{\bar{z}}\right) + \overline{g_2}\left(\frac{R_2^2}{z}\right)\\- \bar{z}\left(\frac{\bar{z}}{R_2^2} - \frac{1}{z}\right)\overline{h_2(z)} - z\left(\frac{z}{R_2^2} - \frac{1}{\bar{z}}\right)h_2(z),\end{aligned} \tag{24}$$

Substituting Eqs. (12), (14), (15), (23), and (24) into Eq. (22), and considering $\overline{\xi}(\xi/R_2^2 - 1/\xi)\overline{h}(\xi) = 0$, we can obtain the following expression:

$$\left\{ g_2(\xi) + g_3\left(\frac{R_2^2}{\overline{\xi}}\right) + (2a+b)[g_2(\xi) + \overline{g_2(\xi)}] \right\}^+$$
$$- \left\{ g_3(\xi) + (1-b)g_2\left(\frac{R_2^2}{\overline{\xi}}\right) - b\overline{g_2}\left(\frac{R_2^2}{\xi}\right) \right\}^-$$
$$= -\frac{\tau^0}{R_2}, \quad |\xi| = R_2, \tag{25}$$

where

$$a = \frac{(2\mu^0 + \lambda^0 - \tau^0)q - 2(\lambda^0 + \tau^0)l}{R_2(4kq - 4l^2)}, \qquad b = \frac{2\mu^0 + \lambda^0 - \tau^0}{4mR_2}.$$

For the current problem, the complex potentials $g_3(z)$ and $h_3(z)$ in the infinite matrix can be taken in the following series forms in accordance to Luo and Chen (1991)

$$g_3(z) = \frac{\gamma}{z - z_0} + \Pi + \frac{\Pi' R_2^2}{z^2} + g_3^*(z), \quad |z| > R_2 \tag{26}$$

$$h_3(z) = \frac{\overline{\gamma}}{z - z_0} + \frac{\gamma \overline{z_0}}{(z - z_0)^2} + \Pi + \frac{\Pi' R_2^2}{z^2} + h_3^*(z), \quad |z| > R_2 \tag{27}$$

where $\gamma = \frac{\mu_3}{\pi(1+\kappa_3)}(b_y - ib_x)$, $g_3^*(z)$ and $h_3^*(z)$ denote the results from the interaction of an edge dislocation with the interphase interface. Π and Π' characterize the remote principal stress field, given as follows in view of Eqs. (11) and (12)

$$4\Pi = \sigma_{11}^\infty + \sigma_{22}^\infty, \quad 2\Pi' = \sigma_{22}^\infty - \sigma_{11}^\infty + 2i\sigma_{12}^\infty, \tag{28}$$

where σ_{11}^∞, σ_{22}^∞ and σ_{12}^∞ are the far-field stresses and assumed to be

$$\sigma_{11}^\infty = \sigma_0, \quad \sigma_{22}^\infty = \eta\sigma_0, \quad \sigma_{12}^\infty = 0. \tag{29}$$

here, η is the biaxial ratio characterizing the loading ratio $\sigma_{22}^\infty/\sigma_{11}^\infty$.

In view of Eq. (10), the displacement continuity condition on the exterior circular interface can be written as

$$\left[\frac{\kappa_2}{\mu_2}g_2(\xi) - \frac{1}{\mu_3}\Omega_3(\xi)\right]^+ = \left[\frac{\kappa_3}{\mu_3}g_3(\xi) - \frac{1}{\mu_2}\Omega_2(\xi)\right]^-, \quad |\xi| = R_2, \tag{30}$$

where $\Omega_3(z)$ and $\Omega_2(z)$ are introduced to be

$$\Omega_3(z) = g_3(z) - \frac{R_2^2}{z}\left(\frac{1}{z} - \frac{\overline{z}}{R_2^2}\right)\overline{h_3}\left(\frac{R_2^2}{z}\right), \quad |z| < R_2, \tag{31}$$

$$\Omega_2(z) = g_2(z) - \frac{R_2^2}{z}\left(\frac{1}{z} - \frac{\overline{z}}{R_2^2}\right)\overline{h_2}\left(\frac{R_2^2}{z}\right), \quad |z| > R_2, \tag{32}$$

Taking the complex conjugate of Eqs. (31) and (32) and combining with Eq. (13), we can achieve the expression as

$$h(z) = \frac{R^2}{z^2}\left[g(z) + \overline{\Omega}\left(\frac{R^2}{z}\right) - zg'(z)\right], \tag{33}$$

By virtue of Eqs. (31) and (32), Eq. (30) can be written as

$$\frac{\kappa_2}{\mu_2}g_2(z) - \frac{1}{\mu_3}\Omega_3(z) = \Xi(z), \quad z \in \Gamma_2^+(|z| < R_2), \tag{34}$$

$$\frac{\kappa_3}{\mu_3}g_3(z) - \frac{1}{\mu_2}\Omega_2(z) = \Xi(z), \quad z \in \Gamma_2^-(|z| > R_2), \tag{35}$$

In the above equations,

$$\Xi(z) = \frac{\kappa_3}{\mu_3}\left[\frac{\gamma}{z - z_0} + \Pi + \frac{\Pi' R_2^2}{z^2}\right] + \frac{1}{\mu_3}\left[\frac{\gamma}{z - z^*} - \frac{\gamma}{z} + \frac{\overline{\gamma}}{\overline{z_0}}\frac{z^*(z^* - z_0)}{(z - z^*)^2}\right] + D,$$

and $z^* = R_2^2/\overline{z_0}$. With the aid of Eqs. (32) and (35), the unknown constant D can be obtained:

$$D = -\frac{1}{\mu_2}g_2(0), \tag{36}$$

Note that the complex potential $g_2(z)$ and $\Omega_2(z)$ in the interphase can have the following expansions:

$$g_2(z) = B_0 + \sum_{n=1}^\infty B_n z^n, \quad R_1 < |z| < R_2, \tag{37}$$

$$\Omega_2(z) = C_0 + \sum_{n=1}^\infty C_{-n} z^{-n}, \quad |z| > R_2, \tag{38}$$

Substituting Eqs. (37), (38) and the results derived from Eqs. (34), (35) into Eq. (25) and comparing the coefficients corresponding to the same power terms, the unknown coefficients on the above equations can be evaluated and $h_2(z)$ will be obtained with the aid of Eqs. (33), (37), and (38). In addition, in order to satisfy the displacement continuity conditions at the interfaces $|z| = R_1$ and $|z| = R_2$ simultaneously, the functions $g_2(z)$ and $h_2(z)$ must be compatible, respectively. So the unknown coefficients on the right-hand of Eqs. (37) and (38) can be given

$$C_0 - B_0 = \frac{(1-\alpha)(R_1^2 - R_2^2)}{R_2^2(1 - \alpha + \beta)(2a + b)}\left[-\frac{\tau^0}{R_2} - \frac{\mu_3}{\kappa_3\mu_2}\left(\frac{\gamma}{z_0} + \frac{\gamma z_0}{R_2^2} + \frac{\overline{\gamma}(z^* - z_0)}{R_2^2}\right)\right], \tag{39}$$

$$\overline{B_0} = (2a + b + 1)\left[\frac{\tau^0}{R_2} + \frac{\mu_3}{\kappa_3\mu_2}\left(\frac{\gamma}{z_0} + \frac{\gamma z_0}{R_2^2} + \frac{\overline{\gamma}(z^* - z_0)}{R_2^2}\right)\right], \tag{40}$$

$$C_{-1} = -\frac{\mu_2\kappa_3\gamma}{\mu_3}, \quad C_{-2} = \frac{\mu_2}{\mu_3}\frac{\overline{\gamma}z^*(z^* - z_0)}{z_0} + \frac{\mu_2}{\mu_3}\gamma z^* + \frac{\mu_2\kappa_3}{\mu_3}\Pi' R_2^2,$$
$$C_{-n} = 0 \quad (n \geqslant 3), \tag{41}$$

$$\overline{B_n} = -\frac{\mu_3}{\kappa_3\mu_2 R_2^{2n}}C_{-n} - \frac{\gamma}{\kappa_3}\delta_{1n} + \frac{\Pi'}{1 - b}\delta_{2n} \quad (n \geqslant 1), \tag{42}$$

$$B_n = -\frac{2a + b}{2a + b + 1}\overline{B_n}, \tag{43}$$

here δ_{ij} is the Kronecker delta.

The expressions of the complex potentials $g_3(z)$ and $h_3(z)$ can be easily calculated from Eqs. (33)–(38)

$$g_3(z) = \frac{\gamma}{z - z_0} + \Pi + \frac{\Pi' R_2^2}{z^2} + \frac{\mu_3}{\kappa_3\mu_2}(C_0 - B_0) + \frac{\mu_3}{\kappa_3\mu_2}\sum_{n=1}^\infty C_{-n}z^{-n}$$
$$+ \frac{1}{\kappa_3}\left[\frac{\gamma}{z - z^*} - \frac{\gamma}{z} + \frac{\overline{\gamma}}{\overline{z_0}}\frac{z^*(z^* - z_0)}{(z - z^*)^2}\right], \quad |z| > R_2, \tag{44}$$

$$h_3(z) = \frac{R_2^2}{z^2}\left\{\frac{\mu_3}{\kappa_3\mu_2}(C_0 - B_0) + \frac{(\kappa_2 - 1)\mu_3}{\mu_2}\overline{B_0} + (1 - \kappa_3)\Pi \right.$$
$$- \frac{\kappa_3\overline{\Pi'}z^2}{R_2^2} + \frac{3\Pi' R_2^2}{z^2} + \frac{\mu_3}{\kappa_3\mu_2}\sum_{n=1}^\infty C_{-n}(n+1)z^{-n} + \frac{\kappa_2\mu_3}{\mu_2}\sum_{n=1}^\infty \overline{B_n}R_2^{2n}z^{-n}$$
$$+ \frac{\gamma}{z - z_0} + \frac{\gamma z}{(z - z_0)^2} + \frac{\kappa_3\overline{\gamma}}{R_2^2}\frac{z^*z}{z - z^*} + \frac{1}{\kappa_3}\left[-\frac{\gamma z^*}{(z - z^*)^2} + \frac{\overline{\gamma}}{\overline{z_0}}\frac{z^*(z_0 - z^*)(z + z^*)}{(z - z^*)^3}\right]$$
$$\left. - \frac{\overline{\gamma}z}{R_2^2} + \frac{\overline{\gamma}}{R_2^2}\frac{z_0 z}{z - z_0} + \frac{\gamma}{R_2^2}\frac{z^2(\overline{z} - \overline{z_0})}{(z - z_0)^2}\right\}, \quad |z| > R_2. \tag{45}$$

3. The plastic flow occurring around the reinforcement and an analysis of the dislocation emission

As mentioned in the introduction, very large stresses may arise in the interface when CNT-reinforced MMNCs fabricated by current processing techniques, as a result of a "misfit" between matrix and CNT due to significant thermal expansion, material properties or microstructural mismatch. In most cases, these stresses may be relaxed by the generation and motion of dislocations in the matrix. Since the activities of conventional dislocation sources are suppressed in nanoscale grains, AIBs or ACIs may possible to become the sources that emit lattice dislocations in deformed MMNCs. However, the micromechanism of dislocations emitted from AIBs or ACIs is unclear. At the same time, such a micromechanism is of importance for understanding the essentials of plastic flow and its transfer from amorphous interphase to adjacent crystalline in MMNCs (Bobylev et al., 2009). In this paper, in order to analyze the effect of coated CNT on the edge dislocations and discuss the plastic flow occurring around the reinforcement, particular attention only paid on the dislocations nucleated at ACIs, i.e., the interface of the amorphous interphase with the metal matrix. Within the theoretically model (Bobylev et al., 2009) and atomic simulation (Wang et al. (2007)), we consider a typical fragment of CNT-reinforced MMNCs consisting of one MWCNT and grains divided by AIBs and ACIs, schematically shown in Fig. 2. When the remote biaxial load is applied, plastic shear initially occurs in ACIs along the plane with θ relative to x-axis (Lubarda, 2011). The plastic flow is assumed to be carried by local shear events occurring in the amorphous interphase. The local shear events are the shear transformations of local atomic clusters, which can act as carriers of plastic flow in amorphous materials (Demkowicz and Argon, 2005). In this case, edge dislocations are generated at ACIs, according to the theory of dislocations (Hirth and Lothe, 1982). The Burgers vector magnitudes of the dislocations gradually increase with the growth of the magnitude of the plastic shear under the remote biaxial load. In particular, one dislocation can split into a residual immobile dislocation that retains at the amorphous interphase and a mobile lattice dislocation that glides into the adjacent grain (Fig. 2c). The glide of the partial dislocation is followed by the formation of stacking fault (wavy line). However, the evaluations of the critical stress for the generation of the dislocations and the direction of the dislocations emission are beyond the scope of this paper. Below, we will investigate mobility and stability of the partial mobile dislocations, because computer simulations demonstrate partial dislocations emitted from ACI in nanocrystalline ceramics (Szlufarska, 2005).

With the case of crystalline materials having grain size $d \geqslant 20$ nm at room temperature, emission of lattice dislocations from ACIs is expected to be the dominant micro-mechanism to accommodate plastic deformation (Kumar et al., 2003). In contrast, in the case of grain size $d < 20$ nm, GB sliding (Bobylev et al., 2010), rotational deformation (Liu et al., 2011b) and diffusional creep (Ovid'ko, 2005) should be taken into consideration when analyzing such problems. So our model only focuses on the metal materials with grain size $d \geqslant 20$ nm. A dislocation model has been proposed to describe the formation and slip of a prismatic circular dislocation loop along the interface between the fiber and the matrix (Gutkin and Ovidko, 2008a,b). So the attention only paid on the dislocations emitted from the amorphous interphase, parallel to the axis of the nanotube and glides along the plane that intersects the nanotube cross-section. In addition, since GBs can act as obstacles to lattice dislocations slip, the dislocations emitted from ACIs are retarded and pile-up at the opposite GBs (see Fig. 1b), which send a back stress and impede further dislocation emission (Wolf et al., 2005; Dao et al., 2007; Kochmann and Le, 2008). For a given
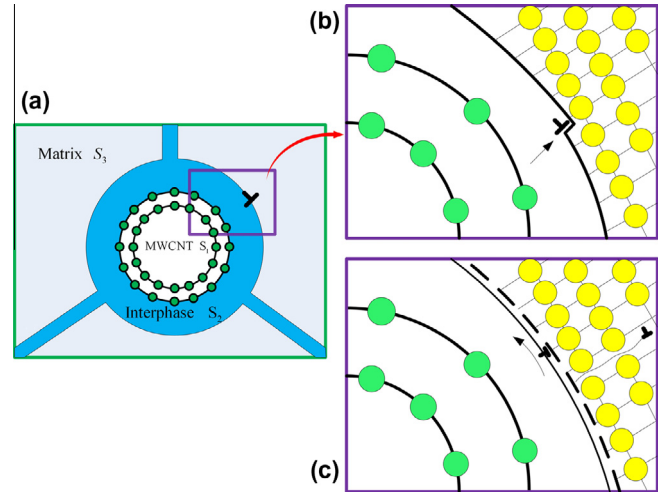

Fig. 2. Generation of an edge dislocation at ACI is accompanied by the emission of a partial dislocation into a nearest crystalline grain in a deformed MMNCs (schematically). (a) Generation of an edge dislocation at the interface; (b) The magnified inset of the part in the wireframe presented in (a); (c) Splitting of the dislocation results in formation of both a mobile partial dislocation that glides in a nearest grain and a residual immobile dislocation. The glide of the partial dislocation is followed by the formation of stacking fault (wavy line).

applied load and grain size, there exists an equilibrium number N_e of dislocations in the pile-ups (Mao and Li, 1999; Wang et al., 2011).

The first dislocation stops at the opposite GB at a distance d (grain size) from the centre of MWCNT. The equilibrium positions and equilibrium numbers of the subsequent dislocations can be calculated by the force balance equations $F_i = 0$, where $i = 2, \cdots, N$ and F_i is the total force acting on the i th dislocation and can be rewritten in the form of $F_i = b\sigma_{r\varphi}^e(r_i, \varphi)$ (Ovid'ko and Sheinerman, 2009). The effective stress $\sigma_{r\varphi}^e(r_i, \varphi)$ is expressed as

$$\sigma_{r\varphi}^e(r_i, \varphi) = \sigma_{r\varphi}^a(r_i, \varphi) + \sigma_{r\varphi}^f(r_i, \varphi) + \sigma_{r\varphi}^{im}(r_i, \varphi)$$
$$+ \sum_{\substack{j=1, \\ j \neq i}}^{N} \sigma_{r\varphi}^d(r_i, r_j, \varphi), \tag{46}$$

where $\sigma_{r\varphi}^a(r_i, \varphi)$ is the shear stress created by the applied macroscopic load; the friction stress $\sigma_{r\varphi}^f(r_i, \varphi)$ is a material property whose magnitude depending on the atomic structure; the image stress $\sigma_{r\varphi}^{im}(r_i, \varphi)$ is associated with the presence of the amorphous phase surface and corresponds to the image force generated by the coated MWCNT; and the stress $\sigma_{r\varphi}^d(r_i, r_j, \varphi)$ is the force exerting on the i th dislocation and created by the j th dislocation at the point (r_i, φ).

In the absence of climb, a prismatic dislocation loop is assumed to glide along its glide cylinder direction. As an interstitial loop moves away from the surface of the inclusion, the lattice friction stress opposes its motion. In the subsequent calculation, the amplitude of lattice friction stress $\sigma_{r\varphi}^f(r_i, \varphi)$ is set equal to $0.001\mu_3$.

If the applied remote stress around the inclusion is a biaxial tension $\sigma_{11}^\infty = \sigma_{22}^\infty$ (i.e., $\eta = 1$), its contribution to the glide force acting on the dislocation is specified by $F^a = b\sigma_{r\phi}^a(r_i, \phi)$. According to transformation formula given by Lubarda (2011), the shear stress $\sigma_{r\varphi}^a(r_i, \varphi)$ along the slip plane can be expressed by the stress components σ_{rr3} and $\sigma_{\theta\theta3}$ as

$$\sigma_i^a = \frac{1}{2}(\sigma_{\theta\theta3} - \sigma_{rr3}) \sin 2(\varphi - \theta), \tag{47}$$

where the polar coordinates φ and θ are given in Fig. 1b and c. By substituting the expression of $\sigma_{\theta\theta3} - \sigma_{rr3}$ obtained from Eqs. (11) and (12) into the above equation, we can achieve

$$\sigma_i^a = \frac{1}{2}\sin 2(\varphi - \theta)\left[g_3(z) + \overline{g_3(z)} + g_3\left(\frac{R_2^2}{\overline{z}}\right) + \overline{g_3}\left(\frac{R_2^2}{z}\right)\right.$$
$$\left. -\overline{z}\left(\frac{\overline{z}}{R_2^2} - \frac{1}{z}\right)\overline{h_3(z)} - z\left(\frac{z}{R_2^2} - \frac{1}{\overline{z}}\right)h_3(z)\right], \tag{48}$$

To be emitted from the ACIs, all dislocations have to overcome the interface attraction zone associated with the existence of the image force $\sigma_{r\varphi}^{im}(r_i,\varphi)$. For the case of only one single dislocation with Burgers vector $B = b_x + ib_y$ located at the point z_0 in the matrix, the image force can be calculated according to the Peach-Koehler formula (Hirth and Lothe,1982; Fang and Liu, 2006), and can be rewritten as

$$f_x - if_y = \frac{\mu_3(b_y^2 + b_x^2)}{\pi(1 + \kappa_3)}\left[\frac{g_3^*(z_0) + \overline{g_3^*(z_0)}}{\gamma} + \frac{\overline{z_0}g_3^{*\prime}(z_0) + h_3^*(z_0)}{\overline{\gamma}}\right], \tag{49}$$

where f_x and f_y are the image force in the x and y direction, respectively. $g_3^*(z_0)$ and $h_3^*(z_0)$ are the perturbation complex potentials in the matrix, which may be calculated as follows:

$$g_3^*(z_0) = \frac{\mu_3}{\kappa_3\mu_2}(C_0 - B_0) + \frac{\mu_3}{\kappa_3\mu_2}\sum_{n=1}^{\infty}C_{-n}(z_0)^{-n}$$
$$+ \frac{1}{\kappa_3}\left[\frac{\gamma}{z_0 - z^*} - \frac{\gamma}{z_0} - \frac{\overline{\gamma}}{\overline{z_0}}\frac{z^*}{z_0 - z^*}\right], \tag{50}$$

$$g_3^{*\prime}(z_0) = -\frac{\mu_3}{\kappa_3\mu_2}\sum_{n=1}^{\infty}nC_{-n}(z_0)^{-n-1} + \frac{1}{\kappa_3}\left[\frac{\gamma}{(z_0)^2} - \frac{\gamma}{(z_0 - z^*)^2} - \frac{2\overline{\gamma}z^*}{\overline{z_0}(z_0 - z^*)}\right], \tag{51}$$

$$h_3^*(z_0) = \frac{R_2^2}{z_0^2}\left\{\frac{\mu_3}{\kappa_3\mu_2}(C_0 - B_0) + \frac{(\kappa_2 - 1)\mu_3}{\mu_2}\overline{B_0} + (1 - \kappa_3)\Pi\right.$$
$$-\frac{\kappa_3\overline{\Pi'}z_0^2}{R_2^2} + \frac{3\Pi'R_2^2}{z_0^2} + \frac{\mu_3}{\kappa_3\mu_2}\sum_{n=1}^{\infty}C_{-n}(n+1)z_0^{-n}$$
$$+\frac{\kappa_2\mu_3}{\mu_2}\sum_{n=1}^{\infty}\overline{B_n}R_2^{2n}z_0^{-n} + \frac{3\gamma}{z_0} + \frac{\kappa_3\overline{\gamma}}{R_2^2}\frac{z^*z_0}{z_0 - z^*}$$
$$+\frac{1}{\kappa_3}\left[-\frac{\gamma z^*}{(z_0 - z^*)^2} + \frac{\overline{\gamma}}{\overline{z_0}}\frac{z^*(z_0 + z^*)}{(z_0 - z^*)^2}\right] + \frac{\overline{\gamma}z_0}{R_2^2} + \frac{\gamma(\overline{z^*} - \overline{z_0})}{R_2^2}\right\}$$
$$-\Pi - \frac{\Pi'R_2^2}{z_0^2} - \frac{2\overline{\gamma}}{z_0} - \frac{\gamma\overline{z_0}}{z_0^2}. \tag{52}$$

Now, the explicit expressions of the image force for the case of one single edge dislocation located in the infinite matrix can be obtained by Eq. (49) together with Eqs. (50)–(52). Moreover, when the total force is larger enough, more dislocations will be punched out into the matrix. To gain the image force exerting on the leading dislocation by the latter one, we can further employ the superposition of Green's functions to construct the expressions of more parallel edge dislocations in the matrix. Suppose that two parallel edge dislocations with the same Burgers vectors (b_x, b_y) are located in points z_0 and z_1, respectively. The image force acting on the dislocations z_0 by the dislocation z_1 can be given by Eq. (49), but for this situation, according to Fang et al. (2009b), the perturbation complex potentials may be rewritten as

$$g_3^*(z_{1-0}) = \Pi + \frac{\Pi'R_2^2}{z_0^2} + \frac{\mu_3}{\kappa_3\mu_2}(E_0 - D_0) + \frac{\mu_3}{\kappa_3\mu_2}\sum_{n=1}^{\infty}E_{-n}(z_0)^{-n}$$
$$+\frac{1}{\kappa_3}\left[\frac{\gamma_1}{z_0 - z_1^*} - \frac{\gamma_1}{z_0} - \frac{\overline{\gamma_1}}{\overline{z_1}}\frac{z_1^*}{z_0 - z_1^*}\right] + \frac{\gamma_1}{z_0 - z_1}, \tag{53}$$

$$g_3^{*\prime}(z_{1-0}) = -\frac{2\Pi'R_2^2}{z_0^3} - \frac{\mu_3}{\kappa_3\mu_2}\sum_{n=1}^{\infty}nE_{-n}(z_0)^{-n-1}$$
$$+\frac{1}{\kappa_3}\left[\frac{\gamma_1}{(z_0)^2} - \frac{\gamma_1}{(z_0 - z_1^*)^2} - \frac{2\overline{\gamma_1}z_1^*}{\overline{z_1}(z_0 - z_1^*)}\right] - \frac{\gamma_1}{(z_0 - z_1)^2}, \tag{54}$$

$$h_3^*(z_{1-0}) = \frac{R_2^2}{z_0^2}\left\{\frac{\mu_3}{\kappa_3\mu_2}(E_0 - D_0) + \frac{(\kappa_2 - 1)\mu_3}{\mu_2}\overline{D_0} + (1 - \kappa_3)\Pi\right.$$
$$-\frac{\kappa_3\overline{\Pi'}z_0^2}{R_2^2} + \frac{3\Pi'R_2^2}{z_0^2} + \frac{\mu_3}{\kappa_3\mu_2}\sum_{n=1}^{\infty}E_{-n}(n+1)z_0^{-n}$$
$$+\frac{\kappa_2\mu_3}{\mu_2}\sum_{n=1}^{\infty}\overline{D_n}R_2^{2n}z_0^{-n} + \frac{\gamma_1}{z_0 - z_1} + \frac{\gamma_1 z_0}{(z_0 - z_1)^2} + \frac{\kappa_3\overline{\gamma_1}}{R_2^2}\frac{z_1^*z_0}{z_0 - z_1^*}$$
$$+\frac{1}{\kappa_3}\left[-\frac{\gamma_1 z_1^*}{(z_0 - z_1^*)^2} + \frac{\overline{\gamma_1}}{\overline{z_1}}\frac{z_1^*(z_0 + z_1^*)}{(z_0 - z_1^*)^2}\right] - \frac{\overline{\gamma_1}z_0}{R_2^2} + \frac{\overline{\gamma_1}}{R_2^2}\frac{z_0z_1}{z_0 - z_1}$$
$$+\frac{\gamma_1}{R_2^2}\frac{z_0^2(\overline{z_1^*} - \overline{z_1})}{(z_0 - z_1)^2}\right\}, \quad |z| > R_2. \tag{55}$$

where $\gamma_1 = \frac{\mu_3}{\pi(1+\kappa_3)}(b_{1y} - ib_{1x})$ and $z_1^* = R_2^2/\overline{z_1}$, substituting γ_1, z_1 and z_1^* into Eqs. (39)–(43) and replacing γ, z_0 and z^*, then generating $E_0 - D_0$, $\overline{D_0}$, E_{-n}, D_n and $\overline{D_n}$ corresponding to $C_0 - B_0$, $\overline{B_0}$, C_{-n}, B_n and $\overline{B_n}$.

To clearly demonstrate the effect of amorphous interphase on the mobility and stability of dislocations, the image force acting on an edge dislocation without amorphous interphase will also be evaluated, for comparison. The formulas for the stress fields of two-phase composite model are adopted in terms of Fang and Liu (2006) and Fang et al. (2007). The interface conditions also employ Eq. (8). Note that in Eq. (49), the complex potentials $g_3^*(z_0)$ and $h_3^*(z_0)$ in the matrix can have the following series expansions:

$$g_3^*(z_0) = \sum_{n=1}^{\infty}M_{-n}(z_0)^{-n}, \tag{56}$$

$$g_3^{*\prime}(z_0) = -\sum_{n=1}^{\infty}nM_{-n}(z_0)^{-n-1}, \tag{57}$$

$$h_3^*(z_0) = \frac{R_2^2}{z_0^2}\left[\sum_{n=0}^{+\infty}M_{-n}(z_0)^{-n} + \sum_{n=1}^{+\infty}\overline{N_n}R_2^{2n}(z_0)^{-n} + \sum_{n=0}^{+\infty}M_{-n}n(z_0)^{-n}\right.$$
$$\left. + \frac{\gamma(z_0\overline{z_0} - R_2^2)}{R_2^2z_0} + \frac{2\overline{\gamma}z_0}{R_2^2}\right] - \frac{2\overline{\gamma}}{z_0} - \frac{\gamma\overline{z_0}}{z_0^2} \tag{58}$$

The unknown coefficients in the right hand side of Eqs. (56)–(58) can be obtained:

$$M_{-n} = \frac{(a+b)(n-1) + c_2}{c_1}\frac{\overline{\gamma}R_2^{2n}}{(\overline{z_0})^{n+1}} + \frac{(n-a-1) + c_3}{c_1}$$
$$\times\left[\gamma(z^*)^{n-1} - \gamma\delta_{1n} - \frac{\overline{\gamma}z^*(z_0 - z^*)(n-1)(z^*)^{n-2}}{\overline{z_0}}\right], \quad n \geqslant 1, \tag{59}$$

$$N_n = \frac{c_5}{c_4}\frac{\gamma}{(z_0)^{n+1}} + \frac{a + an + c_6}{c_4}$$
$$\times\left[\frac{\overline{\gamma}(z^*)^{n-1}}{R_2^{2n}} - \frac{\overline{\gamma}\delta_{1n}}{R_2^{2n}} - \frac{\gamma z^*(z_0 - z^*)(n-1)(z^*)^{n-2}}{z_0R_2^{2n}}\right], \quad n \geqslant 1, \tag{60}$$

where

$$a = \frac{(2\mu^0 + \lambda^0 - \tau^0)q - 2(\lambda^0 + \tau^0)l}{R_2(4kq - 4l^2)}, \qquad b = \frac{2\mu^0 + \lambda^0 - \tau^0}{4mR_2},$$

$$c_1 = 1 + (a+b)(n-1) + \frac{a(a+b)(1+n)(1-n)}{1 + a + na},$$

$$c_2 = \frac{a(1-n)[(a+b)(1+n) - 1]}{1 + a + na},$$

$$c_3 = \frac{a^2(1+n)(1-n)}{1 + a + na}, \quad c_4 = 1 + a(n+1) + \frac{a(a+b)(1+n)(1-n)}{1 + (a+b)(n-1)},$$

$$c_5 = (a+b)(n+1) - 1 + \frac{(a+b)^2(1+n)(n-1)}{(a+b)(1-n)-1},$$

$$c_6 = \frac{(a+b)(1+n)(1+a-an)}{1+(a+b)(n-1)}.$$

and δ_{ij} is the Kronecker delta.

Then, the detailed expressions of the image force for the two-phase composite model can also be gained by Eq. (49) together with Eqs. (56)–(60).

Now the primary physical interest is paid on the glide component F_G of the image force along the glide direction and the component F_C perpendicular to the Burgers vector direction (climb force), which are given by

$$F_G = f_x \cos\theta + f_y \sin\theta, \tag{61}$$

$$F_C = f_x \sin\theta - f_y \cos\theta. \tag{62}$$

where $\theta = \arctan(b_y/b_x)$, i.e., the glide direction of the dislocations relative to x-axis, as shown in Fig. 1b.

The total force acting on the dislocations can be evaluated by using Eqs. (46)–(55). However, to understand the effect of GBs on the mobility and stability of edge dislocations, the equilibrium numbers N_e of lattice dislocations emitted along the same slip plane will be calculated in the glide direction. First, we must verify the leading dislocation can be emitted from ACI by the critical condition:

$$\sigma_{r\varphi}^a(r_i, \varphi) + \sigma_{r\varphi}^f(r_i, \varphi) + \sigma_{r\varphi}^{im}(r_i, \varphi) > 0, \tag{63}$$

Then, adopting the calculation procedures given by Ovid'ko and Sheinerman (2009), we suppose that the $(N+1)$th dislocation ($N = 1, 2, \ldots$) can emit if there exists a region within the interval $0 < r < d$ where the dislocation is repelled from the ACI. The following inequality should be satisfied in this region:

$$\sigma_{r\varphi}^a(r_i, \varphi) + \sigma_{r\varphi}^f(r_i, \varphi) + \sigma_{r\varphi}^{im}(r_i, \varphi) + \sum_{\substack{j=1,\\j\neq i}}^{N} \sigma_{r\varphi}^d(r_i, r_j, \varphi) > 0. \tag{64}$$

4. Numerical results and discussions

The foregoing theory is applicable to calculate the image force exerting on a single dislocation and equilibrium numbers of multiple parallel dislocations in CNT-reinforced MMNCs, with or without interface effect. In this section, we first apply it to evaluate the image force on one single dislocation, and then move on to examine the mobility and stability of multiple parallel edge dislocations in the metal matrix. In the present physical problem, determination of the image force on the dislocations and the equilibrium positions of the dislocations are highly complicated issues of the material properties of three phases, the thickness of the interphase and the orientation of the Burgers vector. In order to simplify the calculations, we suppose that the leading edge dislocation situates at the point x_0 ($x_0 > R_2$ is a real number) on the positive x-axis. The image force is normalized as $f_G = \pi(1+\kappa_3)F_G /R_2[\mu_3(b_x^2 + b_y^2)]$ and $f_C = \pi(1+\kappa_3)F_C/R_2[\mu_3(b_x^2 + b_y^2)]$, and we define the relative location of the edge dislocation $\rho = x_0/R_2$.

MWCNT-reinforced aluminum matrix composites are analyzed as an illustrative example. The parameters used in the calculations for the composite system are listed as follow. We use the transversely isotropic properties of MWCNT given by Shen and Li (2005) and the elastic constants for the aluminum matrix given by Hirth and Lothe (1982) in the calculation, as shown in Table 1. Without loss of generality, the three-phase composite system is assumed to be subjected to remote uniform loading $\sigma_0 = 0.3\mu_3$, $\eta = 1$ and Burgers vector $b = 0.25$ nm. The interface effect along

the circle Γ_2 is represented by the surface elastic constants μ^0 and λ^0 and the interface residual stress τ^0. Two different cases of interface effect used in the present investigation are equivalent to surface modulus of the aluminum, as shown in Table 2. Although the surface properties are generally anisotropic, the transverse isotropic case is assumed to be sufficient to elaborate the main features of the size-dependent response.

4.1. An analysis of the image force exerting on an edge dislocation

4.1.1. The influence of interface constants and residual stress

As a starting point, we will mainly focus on the comparison of the image force obtained by adopting the three-phase composite cylinder model and the two-phase composite model, with three different sets of interface properties and interface residual stresses when a single edge dislocation located in the matrix by utilizing Eqs. (49)–(52) and Eqs. (56)–(60). The relations of the image force with the radius are plotted in Figs. 3–5 for $\upsilon_2 = \upsilon_3 = 0.34$, $\mu_2/\mu_3 = 1.1$, $R_2 - R_1 = 3$ nm and $\rho = 1.2$. Fig. 3 shows the comparision of the normalized glide/climb force versus the radius R_1 of MWCNT for the case $\tau^0 = 0$. Then the influence of interface residual stress τ^0 upon the image force is depicted in Fig. 4 without considering the interface constants ($\mu^0 = 0, \lambda^0 = 0$). At last, Fig. 5 displays the image force with different radii for three combinations of the interface stress τ^0 and the interface constants μ^0 and λ^0. It is clear from Figs. 3–5 that the model presented in the paper is obviously different from the case that without the amorphous layer. We will discuss the variation of the image force obtained using the three-phase composite cylinder model carefully in the following. For convenience, the interface elastic constants are written as $K^0 = 2\mu^0 + \lambda^0 - \tau^0$, and for the case of $\mu^0 = -5.4251$ N/m, $\lambda^0 = 3.4939$ N/m, $\tau^0 = 0.5689$ N/m, $K^0 = -7.9253$ N/m < 0, while $K^0 = 5.1882$ N/m > 0, for $\mu^0 = -0.3760$ N/m, $\lambda^0 = 6.8511$ N/m, $\tau^0 = 0.9108$ N/m. It can be seen from Figs. 3–5 that, if interface constants are positive ($K^0 > 0$), the normalized climb force f_C is smaller than that in the classical case without considering the interface effect ($K^0 = 0$ in the associated plot has been provided in Fig. 3), while the values of the glide force become larger compared to the corresponding spots in the classical one. However, for the case $K^0 < 0$, the trend is reversed. One feature shared by them was the smaller the radius of MWCNT, the larger discrepancies between the values ($K^0 \neq 0$) and the classical case, especially when the size is below 10 nm. In brief, an additional attractive force or repulsive force will act on the edge dislocation on account of the interface effect, which causes the normalized glide/climb force to decrease or increase. The phenomenon cannot be produced by the classical elasticity solution and agree with the results given by Fang et al. (2009b). This implies that local hardening and softening can occur at the interface due to the presence of the interface effect. In addition, the classical solution ($K^0 = 0, \tau^0 = 0$) in the present paper is dependent on the size of MWCNT. This mainly

Table 1
Parameters used in the calculation of total force acting on the dislocations in CNT-reinforced MMNCs (MWCNT properties taken from Shen and Li (2005) and matrix properties from Hirth and Lothe (1982)).

Elastic constituent properties	MWCNT (phase 1)	Metal matrix (phase 3)
Axial Young's modulus (E_{zz})	1.17 T Pa	–
Transverse bulk modulus ($K_{r\theta}$)	130 GPa	–
Transverse shear modulus ($\mu_{r\theta}$)	5.98 GPa	–
In plane shear modulus (μ_{rz})	277 GPa	–
In plane Poisson's ratio (ν_{rz})	0.139	–
Shear modulus (μ)	–	27 GPa
Poisson's ratio (ν)	–	0.34

Table 2
the surface modulus of aluminum (Miller and Shenoy, 2000; Sharma et al., 2003).

Surface modulus	Al[1 0 0] surface (phase 1)	Al[1 1 1] surface
Surface elastic constants μ^0 (N/m)	−5.4251	−0.3760
λ^0 (N/m)	3.4939	6.8511
Residual surface stress τ^0 (N/m)	0.5689	0.9108

attributes to the position of the edge dislocation is changing in line with the variation of the radius, finally lead to the variation of the glide/climb force with the radius even the interface elastic constants and interface stress are neglected. Through the comparison of the three sets of figures among Figs. 3–5 again, it is concluded

that the interface effect is mainly due to the interface elastic constants μ^0 and λ^0 rather than the interface residual stress τ^0.

4.1.2. The mechanical properties and thickness effect of the amorphous interphase

The normalized glide force f_G and climb force f_C for different values of μ_2/μ_3 versus the relative position ρ are given in Fig. 6 for $\upsilon_2 = \upsilon_3 = 0.34$, $R_1 = 10.19$ nm, $R_2 - R_1 = 3$ nm and $\mu^0 = -5.4251$ N/m, $\lambda^0 = 3.4939$ N/m, $\tau^0 = 0.5689$ N/m. It can be seen from Fig. 6 that the glide force is always negative expect for one single point. In other words, the coated MWCNT attracts the edge dislocation in the matrix under the given condition all the time, regardless of the value μ_2/μ_3 larger than 1 or not. It is clearly different from the classical elasticity result, in which the stiff
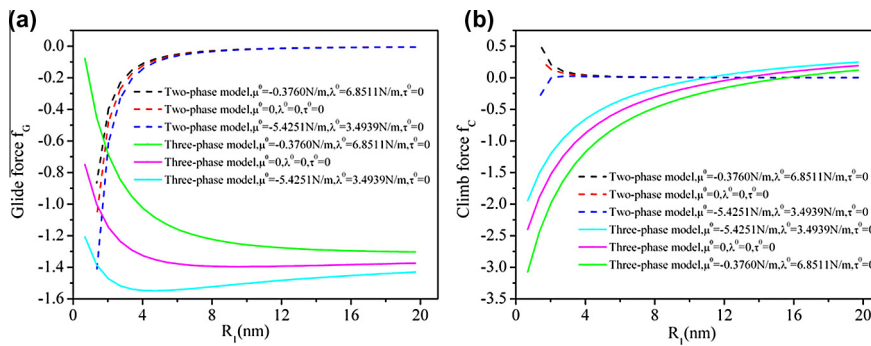
Fig. 3. Comparison of the image force f_G and f_C as a function of the radius R_1 of MWCNT for $\upsilon_2 = \upsilon_3 = 0.34$, $\mu_2/\mu_3 = 1.1$, $R_2 - R_1 = 3$ nm, $\rho = 1.2$, for (a) glide force $f_G (b_y = 0)$ and (b) climb force f_C $(b_x = 0)$ under the condition $\tau^0 = 0$.
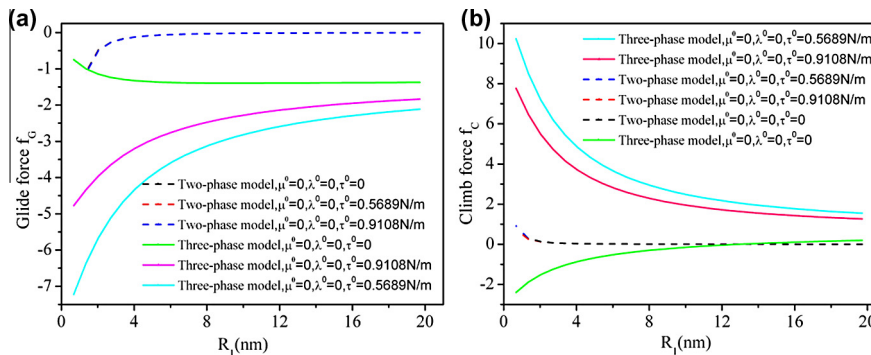

Fig. 4. Comparison of the image force f_G and f_C as a function of the radius R_1 of MWCNT for $\upsilon_2 = \upsilon_3 = 0.34$, $\mu_2/\mu_3 = 1.1$, $R_2 - R_1 = 3$ nm, $\rho = 1.2$, for (a) glide force $f_G (b_y = 0)$ and (b) climb force f_C $(b_x = 0)$ for the influence of interface stress τ^0 without the surface constants ($\mu^0 = 0$, $\lambda^0 = 0$).
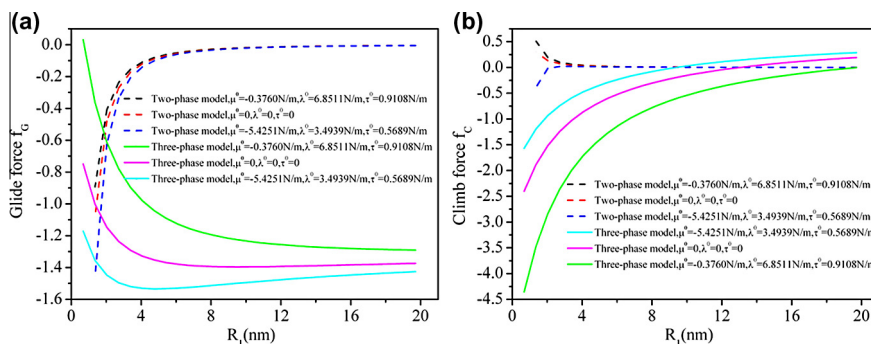

Fig. 5. Comparison of the image force f_G and f_C as a function of the radius R_1 of MWCNT for $\upsilon_2 = \upsilon_3 = 0.34$, $\mu_2/\mu_3 = 1.1$, $R_2 - R_1 = 3$ nm, $\rho = 1.2$, for (a) glide force $f_G (b_y = 0)$ and (b) climb force f_C $(b_x = 0)$ for combinations of the interface stress τ^0 and the interface constants μ^0 and λ^0..

inclusion ($\mu_2/\mu_3 > 1$) will always repel the edge dislocation lied near the inclusion within the matrix. This happen may because of the combined effect of negative interface elastic constant, interface stress and the amorphous interphase. This phenomenon is similar to the micrographs (Schröder and Arzt, 1985), which give the impression of an attractive interaction between the particles and dislocations. In addition, the attractive interaction of a mobile lattice dislocation with a larger particle is also illustrated by a series of images (Clark et al., 2005). Moreover, a strong attractive interaction is obtained by adopting linear elasticity theory and the evaluated glide force is always negative when the dislocation locates at the positive y−axis. In the glide direction, the amorphous interphase will always attract the edge dislocations in the matrix, which can cause local hardening at the ACI. It can be concluded that for negative interface characteristic constants ($K^0 < 0$), there exists significant local hardening at the interface between the amorphous layer and the matrix, whether the coating layer harder or softer than the matrix. Additionally, an interesting result found in Fig. 6 is that for the case $\mu_2/\mu_3 \leqslant 1.1$, the normalized climb force is positive first, and then becomes negative. The equilibrium positions of the dislocation can be obtained by letting the image force on dislocation zero. When the relative position increases to a critical value (about 1.5), there is a stable equilibrium position. However, no equilibrium position is available for $\mu_2/\mu_3 = 1.5$, 3 or 5. This may attribute to the fact that as the ratio of relative shear modulus μ_2/μ_3 decreases, the same value of the elastic constants of MWCNT has a more pronounced influence on the climb force. For small values of the relative position, the repulsive force created by the stiff reinforcement and interphase overcomes the attractive force produced by the interface constants, interface stress and amorphous interphase, which lead to the change of the direction of the climb force. The discrepancies between the normalized climb forces disappear gradually with increases of relative position. Generally speaking, inserting an amorphous interphase between the stiff reinforcement and the soft matrix provides a possible method to achieve significant local hardening at the interface with considering the negative interface effect.

Then we change Poisson's ratio of the coating layer instead of shear modulus. We can achieve the relationship between the glide force f_G and the climb force f_C with different values of υ_2. The variations of the image force as a function of the relative location ρ are depicted in Fig. 7 for $\mu_2/\mu_3 = 1.1$, $R_1 = 10.19$ nm, $R_2 - R_1 = 3$ nm and $\mu^0 = -5.4251$ N/m, $\lambda^0 = 3.4939$ N/m, $\tau^0 = 0.5689$N/m. The variations of the glide force have the same trend along with the change of Poisson's ratio υ_2, and opposite trend can be seen for the climb force. The conclusions parallel to those drawn in Fig. 6. In addition, when $\upsilon \leqslant 0.4$, there exist two equilibrium positions
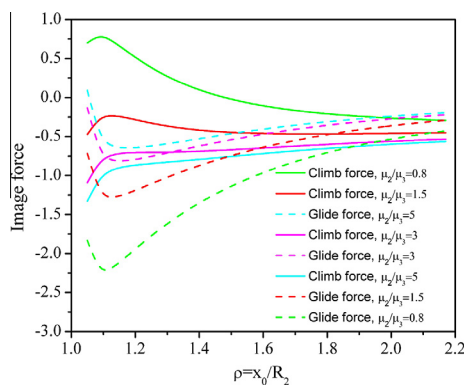
of the edge dislocation (one stable and the other one unstable) on the x-axis where the climb forces equal to zero at these points. Similar observation has been given in a theoretical model describing the mobility of a misfit dislocation dipole in a wire composite including a hard cylindrical substrate coated by a soft co-axial cylindrical film (Wang et al., 2010). It is concluded from these figures that the variation of Poisson's ratio of the amorphous interphase also can affect the stability of the dislocation, especially in the climb direction.

We will examine the thickness effect of the interphase on the image force acting on the dislocation in the following part. The normalized glide force f_G and the normalized climb force f_C for different thicknesses are plotted in Fig. 8 ($b_y = 0$) and Fig. 9 ($b_x = 0$), respectively, for $\mu_2/\mu_3 = 1.1$, $\upsilon_2 = \upsilon_3 = 0.34$, $\rho = 1.2$ and $\mu^0 = -5.4251$ N/m, $\lambda^0 = 3.4939$ N/m, $\tau^0 = 0.5689$N/m. It is clearly seen from Fig. 8 that when the thickness $R_2 - R_1$ of the interphase is small, the glide force varies widely, especially in the region where the size of MWCNT is close to the thickness of the amorphous interphase. However, when $R_2 - R_1$ is large (the MWCNT is thickly coated), the glide force increases linearly at a set ratio with the size of the amorphous interphase increases. It can be found from Fig. 9 that when the thickness of interphase is small, the climb force is negative first, and then becomes positive with large size of MWCNT. There exists an unstable equilibrium. However, with increases of the thickness, the climb force will always be positive and the values changeless with the variation of the size of the MWCNT. Roughly speaking, the thinner the thickness of the amorphous interphase, the larger the effect of climb force. From Figs. 8 and 9, we conclude that when the thickness of the interphase is small and approximate to the radius of the reinforcement, the coated MWCNT has vital influence on the image force exerting on the edge dislocation. In contrast, when the amorphous interphase is thick enough, the image force increases slightly with increases of the radius of MWCNT. The results agree with the investigation finished by Xiao and Chen (2001) that as the thickness of the coating layer increases, the influence of the MWCNT on the mobility of the dislocation may be shielded. In other words, when the interphase is thick enough, the elastic properties of the inclusion and the interface stresses have not-so-obvious influence on the force exerting on the dislocations.

4.1.3. Size effect of MWCNT

To analyze the size (radius) effect of MWCNT on the image force, Figs. 10 and 11 exhibit the glide force f_G and climb force f_C as a function of the relative location $\rho = x_0/R_2$ for $\mu_2/\mu_3 = 1.1$, $\upsilon_2 = \upsilon_3 = 0.34$, $R_2 - R_1 = 3$ nm and $\mu^0 = -5.4251$ N/m, $\lambda^0 = 3.4939$ N/m, $\tau^0 = 0.5689$ N/m, respectively. It is clearly seen from
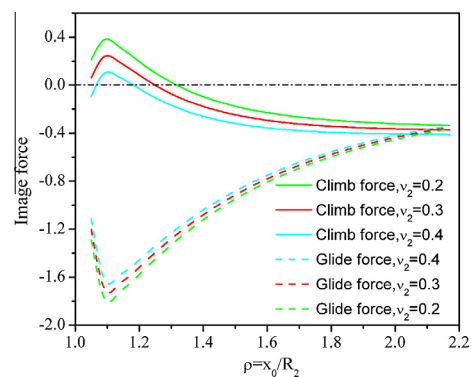

Fig. 6. Glide force f_G and Climb force f_C vs. the relative location $\rho = x_0/R_2$ for $\upsilon_2 = \upsilon_3 = 0.34$, $R_1 = 10.19$ nm, $R_2 - R_1 = 3$ nm and $\mu^0 = -5.4251$ N/m, $\lambda^0 = 3.4939$ N/m, $\tau^0 = 0.5689$ N/m.

Fig. 7. Glide force f_G and Climb force f_C as a function of the relative location $\rho = x_0/R_2$ for $\mu_2/\mu_3 = 1.1$, $R_1 = 10.19$ nm, $R_2 - R_1 = 3$ nm and $\mu^0 = -5.4251$ N/m, $\lambda^0 = 3.4939$ N/m, $\tau^0 = 0.5689$ N/m.

Fig. 10 that the size effect of MWCNT on the glide force becomes negligible when the relative position of the edge dislocation beyond the critical value $\rho = 1.2$. In contrast, the size effect is quiet evident when the dislocation near the ACI, and the values of f_G diminish extremely rapidly as ρ from origin close to 1.2, especially in the case of small radius. In the climb direction, the influence of size on the image force exhibits different features, as shown in Fig. 11. Nevertheless, the climb forces tend towards stability with increases of the relative location, as well as the glide force. It implies that the size effect of MWCNT on the mobility and stability of the edge dislocation is significant within certain realms in metal matrix.

4.1.4. The effect of the orientation of the Burgers vector

Figs. 12 and 13 elaborate the glide force f_G and the climb force f_C as functions of the direction of the Burgers vector θ for $v_2 = v_3 = 0.34$, $\mu_2/\mu_3 = 1.1$, $R_1 = 10.19$ nm, $R_2 - R_1 = 3$ nm and $\rho = 1.2$. At $\theta = 0^0$, the normalized glide force reduces for negative K^0 and increases for positive K^0 when compared to the classical result. The glide force is equal to zero for all cases at $\theta = 90^0$. It is also found from Fig. 12 that the glide force is negative first and equals zero around $\theta = 30^0$, then becomes positive with increases angle θ for classical solution ($K^0 = 0$). However, if the interface constants are considered, the absolute value of the glide force is smaller than that for classical solution at the majority distribution of θ. The influence of the interface stress upon the glide force is largest when the angle is approximate 60^0, while the influence is almost negligible when $\theta \leqslant 15^0$. We can see from Fig. 13 that the climb force f_C is always negative for classical solution and the case considering the interface properties (for the case $K^0 > 0$). The values of climb force below zero when $\theta = 0^0$, mainly because of the existence of remote uniform loadings. Looking at a close-up of the classical solution, we can observe distinct troughs are adjacent to the angle $\theta = 35^0$, when the effect of the interface stress on the climb force is the largest, and after that the magnitude of the climb force decreases with the angle increases. The discrepancy of these two kinds of interface effect is also found to be unremarkable when compared to the classical solution, mainly due to the interface constant $\mu^0 < 0$ in both cases regardless of $K^0 > 0$ or not. From the results obtained, it seems that the presence of the interface stress has significant influence on the glide force and climb force when the direction of the Burgers vector varies.

4.2. Analysis of dislocation stability

In this section, attention is paid on the total glide/climb force acting on the subsequent edge dislocations and the impact of the interface conditions and elastic mismatch of three phases on the equilibrium numbers of the dislocations at a given size grain. For
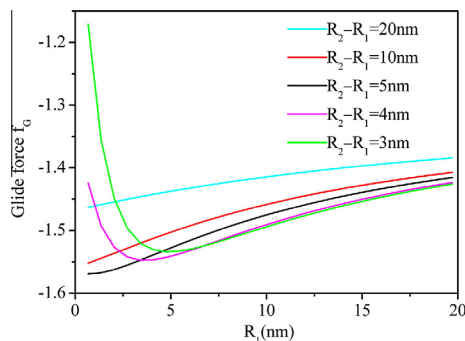

Fig. 9. Climb force f_C as a function of the radius R_1 for $\mu_2/\mu_3 = 1.1$, $v_2 = v_3 = 0.34$, $\rho = 1.2$ and $\mu^0 = -5.4251$ N/m, $\lambda^0 = 3.4939$ N/m, $\tau^0 = 0.5689$ N/m ($b_x = 0$).
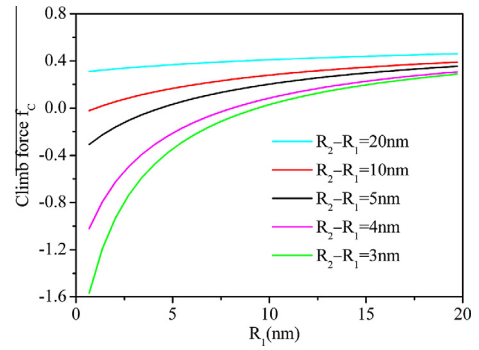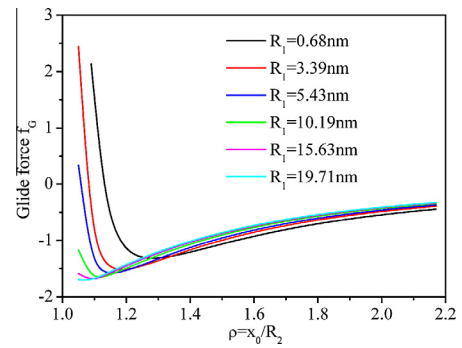

Fig. 10. Glide force f_G as a function of the relative location $\rho = x_0/R_2$ for $\mu_2/\mu_3 = 1.1$, $v_2 = v_3 = 0.34$, $R_2 - R_1 = 3$ nm and $\mu^0 = -5.4251$ N/m, $\lambda^0 = 3.4939$ N/m, $\tau^0 = 0.5689$ N/m ($b_y = 0$).
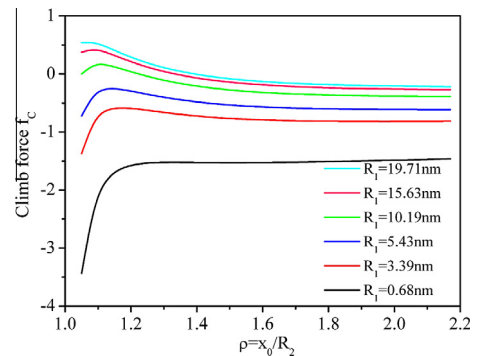

Fig. 11. Climb force f_C as a function of the relative location $\rho = x_0/R_2$ for $\mu_2/\mu_3 = 1.1$, $v_2 = v_3 = 0.34$, $R_2 - R_1 = 3$ nm and $\mu^0 = -5.4251$ N/m, $\lambda^0 = 3.4939$ N/m, $\tau^0 = 0.5689$ N/m ($b_x = 0$).

comparison's sake, in subsequent numerical calculation, we define the normalized stress $f_0 = \pi(1 + \kappa_3)f/R_2[\mu_3(b_x^2 + b_y^2)]$, where $f = \sigma_{r\varphi}^a(r_i, \varphi)$, $\sigma_{r\varphi}^f(r_i, \varphi)$ or $\sigma_{r\varphi}^d(r_i, \varphi)$, respectively. The repulsive portion of the total glide force is mainly due to applied stress, while the attractive portion consists of the image force, friction stress and the interactions between neighbor dislocations. In Figs. 14 and 15, the variation of the total force with respect to the parameter R_1 for the leading dislocation is illustrated with $v_2 = v_3 = 0.34$, $\mu_2/\mu_3 = 1.1$, $R_2 - R_1 = 3$ nm, $\theta = 30^0$ and $\rho = 1.2$. It is found from Fig. 14 that the total glide force is always positive when incorporating the interface effect, while the force is negative for the classical case. Parallel result can be found in Fig. 15 for the total climb force. When the interface effect is taken into consideration, the
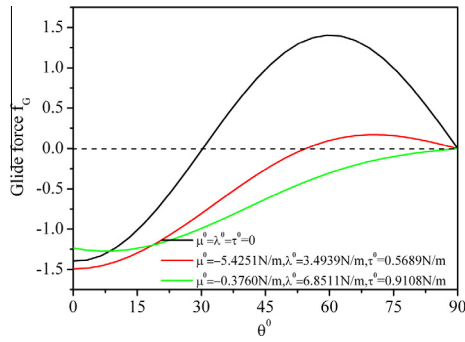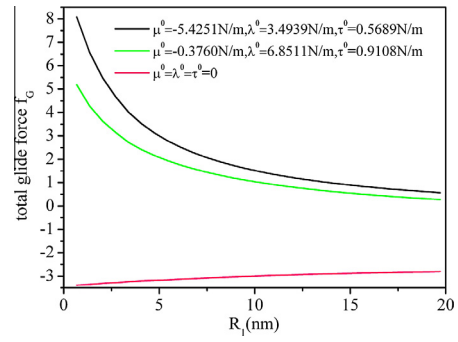

Fig. 8. Glide force f_G as a function of the radius R_1 for $\mu_2/\mu_3 = 1.1$, $v_2 = v_3 = 0.34$, $\rho = 1.2$ and $\mu^0 = -5.4251$ N/m, $\lambda^0 = 3.4939$ N/m, $\tau^0 = 0.5689$ N/m ($b_y = 0$).

Fig. 12. Glide force f_G vs. the direction of the Burgers vector θ for $\upsilon_2 = \upsilon_3 = 0.34$, $\mu_2/\mu_3 = 1.1$, $R_1 = 10.19$ nm, $R_2 - R_1 = 3$ nm and $\rho = 1.2$.

Fig. 13. Climb force f_C vs. the direction of the Burgers vector θ for $\upsilon_2 = \upsilon_3 = 0.34$, $\mu_2/\mu_3 = 1.1$, $R_1 = 10.19$ nm, $R_2 - R_1 = 3$ nm and $\rho = 1.2$.

Fig. 14. The value of the total glide force as a function of the relative position $\rho = x_0/R_2$ for $\mu_2/\mu_3 = 1.1$, $\upsilon_2 = \upsilon_3 = 0.34$, $R_1 = 10.19$ nm, $R_2 - R_1 = 3$ nm and $\theta = 30^0$.

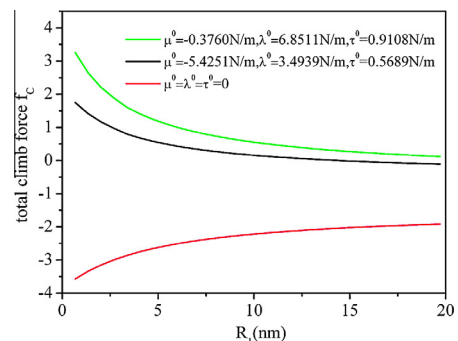**Fig. 15.** The value of the total climb force as a function of the relative position $\rho = x_0/R_2$ for $\mu_2/\mu_3 = 1.1$, $\upsilon_2 = \upsilon_3 = 0.34$, $R_1 = 10.19$ nm, $R_2 - R_1 = 3$ nm and $\theta = 30^0$.
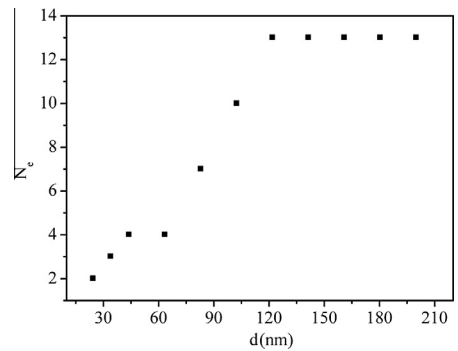

Fig. 16. The equilibrium numbers N_e of edge dislocations that can be emitted from the ACI along the same slip plane as a function of grain size d in nanocrystalline Al.

inequality (63) is satisfied. Then the first dislocation can be emitted from the ACI and move far away. We can also conclude that the emission of edge dislocation from the ACI is difficult for the classical case. The absolute values of the glide/climb force increases rapidly with decreases of the radius of MWCNT. This is the so-called "smaller but stronger". In short, the smaller the radius, the larger relative thickness of amorphous interphase to the size of MWCNT is presented. As a result, the influence of amorphous interphase and interface effect on the dislocations stability is remarkable. Then the equilibrium numbers of dislocations along the same slip direction with considering the interface effect will be evaluated.

To investigate the effect of GBs on the stability of the edge dislocations, the maximum numbers N_e of lattice dislocations along the same slip plane is calculated by adopting the computational procedure in Section 3. For definiteness, we put $\mu_2/\mu_3 = 1.1$, $\upsilon_2 = \upsilon_3 = 0.34$, $R_1 = 10.19$ nm, $R_2 - R_1 = 3$ nm and $\theta = 30^0$. The variation of N_e with grain size d is shown in Fig. 16. It can be clearly seen that fewer dislocations can be emitted from the ACI at a smaller size grain. In particular, when the grain size of crystalline materials less than 100 nm, i.e., in nanocrystalline matrix, the dislocations emitted from the ACI is quietly low. With the grain size decreases, the distance between ACI and GB becomes closer. So the stress $\sigma_{r\varphi}^d(r_i, r_j, \varphi)$ created by the previous dislocations will inhibit the subsequent dislocations. This means that, dislocations will not easily be emitted from ACI for small grain size, which in turn inhibits the delamination of the interface between the reinforcement and matrix. Another interesting appearance shown in Fig. 16 is that the equilibrium numbers of dislocations seem to be insensitive to the large grain size. From the expression (46), the equilibrium numbers is determined by four factors: $\sigma_{r\varphi}^f(r_i, \varphi)$, $\sigma_{r\varphi}^{im}(r_i, \varphi)$ and $\sigma_{r\varphi}^d(r_i, r_j, \varphi)$, of which $\sigma_{r\varphi}^a(r_i, \varphi)$ is beneficial for the emission of dislocations. Since value of the shear stress

is very small far away from the coated MWCNT, the mobility of dislocations becomes more difficult.

5. Conclusions

The effect of the interaction between the amorphous interphase and edge dislocations on the local plastic behavior of CNT-reinforced MMNCs is presented in the paper. The influence of amorphous interphase and interface conditions on the interaction between edge dislocations and a circular nanoscale coated MWCNT are comparatively complicated issues, for there are many factors that can affect the mobility and stability of dislocations. These

include interface effect, materials properties of coated MWCNT and orientation of the Burgers vector, among others. A three phase composite cylinder model is developed to explain the new boundary value problem. In addition, the plastic flow occurring around the reinforcement and the emission of edge dislocations from the amorphous interphase is addressed. The image force acting on an edge dislocation is evaluated in detail, and the image force evaluated in the three phase composite cylinder model is obviously different from that calculated in the two-phase composite model without the amorphous interphase. The interface conditions are proved to have significant effect on the glide/climb force acting on an edge dislocation when the size of MWCNT is very small, typically approximate ten nanometers. An additional repulsive force or attractive force exerts on the edge dislocation due to the existence of interface effect. An amorphous interphase existing between the stiff reinforcement and the soft matrix can achieve significant local hardening at the interface with considering the negative interface effect. However, when the amorphous interphase is thick enough, the influences of the interface stresses and the elastic constants of the reinforcement on the glide/climb force are slight. With the variation of the direction of Burgers vector, the effect of interface stress on glide/climb force is significant. In addition, the elastic interaction between two edge dislocations may be strongly affected by interface conditions and nearby nano-sized coated reinforcement. At last, the equilibrium numbers of edge dislocations are presented by numerical procedures and discussed in detail. It is found that the equilibrium numbers of dislocations are sensitive to the grain size, especially for nanocrystalline. These solutions may form the basis for problems of significant crack-inclusion interaction relevant to composite materials, especially for CNT-reinforced MMNCs (Kim and Sudak, 2005). Such investigation may provide some insight into determining the optimal coated CNT cross-section of CNT-reinforced MMNCs; estimating the difference in performance due to deviations from the optimum. Additionally, these solutions can be useful for studying the generation and growth of crack, as well as the overall elastic and plastic properties in CNT-reinforced MMNCs.

In retrospect, it must be recognized that the adoption of circular coherent interface is an idealizations in this development. With semi-coherent or incoherent interfaces, the jump of the interfacial strain in the adjoining bulk materials is required (Romanov and Wagner, 2001). Additionally, Incorporation of the interatomic potential is another desirable route to model CNT, interphase and interface effects, though involving a higher degree of calculation complexity (Jiang et al., 2006; Tan et al., 2007; Wu et al., 2009; Pavia and Curtin, 2011). The constitutive properties of interphase can be derived from atomistic simulations and then introduced in a continuum micromechanics-based interphase model to characterize the macroscopic plastic behaviors of nanocomposites considering the effect of surface/interface stress (Zhang et al., 2010; Azizi et al., 2011; Paliwal and Cherkaoui, 2012). Such an approach could link the discrete atomic level interactions and continuum mechanics (Espinosa et al., 2006), and it is expected to tailor it specifically to CNT-reinforced materials. Further study of these and other factors deserve to be implemented in the future.

Acknowledgements

Appendix A. Explicit evaluation of the complex analytical functions $h_1(z)$ and $h_2(z)$ in Eqs. (18) and (19)

With the aid of the continuation theory given by England (1971), it can be demonstrated from Eq. (16) that the function $\phi(z) = g_1(z) + g_2(z)$ is holomorphic in the finite region $R_1^2/R_2 < |z| < R_2$. Therefore, we can express $\phi(z)$ according to Xiao and Chen (2001) as

$$\phi(z) = -\overline{g_1}(0) + \sum_{n=-\infty}^{+\infty} A_n z^n, \quad R_1^2/R_2 < |z| < R_2, \tag{A.1}$$

Since $\phi(z) = g_1(z) + g_2(z)$, by virtue of Eq. (16) and eliminating $g_2^+(z)$ and $g_2^-(z)$, Eq. (17) will be reduced to the Hilbert problem.

$$g_1^+(z) + \alpha g_1^-(z) = \beta \phi(z), \tag{A.2}$$

where the two parameters α and β are defined by

$$\alpha = \frac{\kappa_2 \mu_1 + \mu_2}{\kappa_1 \mu_2 + \mu_1}, \quad \beta = \frac{(\kappa_2 + 1)\mu_1}{\kappa_1 \mu_2 + \mu_1}, \tag{A.3}$$

Introducing a sectionally holomorphic auxiliary function, $\Psi(z)$ is defined by

$$\Psi(z) = \begin{cases} g_1(z) - (\alpha - \beta)\overline{g_1}(0) - \beta \sum_{n=0}^{+\infty} A_n z^n, & |z| < R_1, \\ -\alpha g_1(z) - \alpha \overline{g_1}(0) + \beta \sum_{n=1}^{+\infty} A_{-n} z^{-n}, & |z| > R_1. \end{cases} \tag{A.4}$$

Obviously, $\Psi(z)$ is analytic and single value in the whole complex plane even containing the points at infinity. By Liouville's theorem, $\Psi(z)$ must be constant and is identically equal to zero, i.e.

$$\Psi(z) \equiv 0. \tag{A.5}$$

Hence we can obtain the following expressions

$$g_1(z) = (\alpha - \beta)\overline{g_1}(0) + \beta \sum_{n=0}^{+\infty} A_n z^n, \quad |z| < R_1, \tag{A.6}$$

$$g_1(z) = -\overline{g_1}(0) + \frac{\beta}{\alpha} \sum_{n=1}^{+\infty} A_{-n} z^{-n}, \quad |z| > R_1, \tag{A.7}$$

From Eq. (A.6), we can determine $\overline{g_1}(0)$ and $g_1(0)$ as

$$\overline{g_1}(0) = \frac{(\alpha - \beta)\beta A_0 + \beta \overline{A_0}}{1 - (\alpha - \beta)^2}, \quad g_1(0) = \frac{(\alpha - \beta)\beta \overline{A_0} + \beta A_0}{1 - (\alpha - \beta)^2}, \tag{A.8}$$

Subtracting the above expressions (A.6) and (A.7) from Eq. (A.1) and achieving the following expressions:

$$g_2(z) = -(1 + \alpha - \beta)\overline{g_1}(0) + \sum_{n=1}^{+\infty} A_{-n} z^{-n} + (1 - \beta) \sum_{n=0}^{+\infty} A_n z^n,$$
$$R_1^2/R_2 < |z| < R_1, \tag{A.9}$$

$$g_2(z) = \sum_{n=0}^{+\infty} A_n z^n + \left(1 - \frac{\beta}{\alpha}\right) \sum_{n=1}^{+\infty} A_{-n} z^{-n}, \quad R_1 < |z| < R_2, \tag{A.10}$$

Then, substituting Eqs. (A.6) and (A.10) into Eq. (13) with $R = R_1$ lead to

$$h_1(z) = \frac{R_1^2}{z^2} \left[\frac{\beta}{\alpha} \sum_{n=1}^{+\infty} \overline{A_{-n}} \left(\frac{z}{R_1^2}\right)^n - \beta \sum_{n=1}^{+\infty} A_n (n-1) z^n \right], \quad |z| < R_1, \tag{A.11}$$

$$h_2(z) = \frac{R_1^2}{z^2}\left[\frac{1-\alpha}{1-\alpha+\beta}(A_0+\overline{A_0}) - \sum_{n=1}^{+\infty}A_n(n-1)z^n + \sum_{n=1}^{+\infty}\overline{A_{-n}}\left(\frac{z}{R_1^2}\right)^n\right.$$
$$\left.+(1-\beta)\sum_{n=1}^{+\infty}\overline{A_n}\left(\frac{R_1^2}{z}\right)^n + \left(1-\frac{\beta}{\alpha}\right)\sum_{n=1}^{+\infty}A_{-n}(n-1)z^{-n}\right],$$
$$R_1 < |z| < R_2. \tag{A.12}$$

References

Aghababaei, R., Joshi, S.P., 2013. Micromechanics of crystallographic size-effects in metal matrix composites induced by thermo-mechanical loading. Int. J. Plast. 42, 65–82.

Ahmad, I., Unwin, M., Cao, H., Chen, H., Zhao, H., Kennedy, A., Zhu, Y.Q., 2010. Multi-walled carbon nanotubes reinforced Al₂O₃ nanocomposites: Mechanical properties and interfacial investigations. Compos. Sci. Technol. 70, 1199–1206.

Ashby, M.F., 1966. Work hardening of dispersion-hardened crystals. Philos. Mag. 14, 1157–1178.

Azizi, R., Niordson, C.F., Legarth, B.N., 2011. Size-effects on yield surfaces for micro reinforced composites. Int. J. Plast. 27, 1817–1832.

Bakhshayesh, H.A., Gutkin, M.Y., Shodja, H.M., 2012. Surface/interface effects on elastic behavior of a screw dislocation in an eccentric core–shell nanowire. Int. J. Solids Struct. 49, 1665–1675.

Bakshi, S.R., Lahiri, D., Agarwal, A., 2010. Carbon nanotube reinforced metal matrix composites - a review. Int. Mater. Rev. 55, 41–64.

Balani, K., Agarwal, A., 2008. Wetting of carbon nanotubes by aluminum oxide. Nanotechnology 19, 165701–165709.

Barai, P., Weng, G.J., 2011. A theory of plasticity for carbon nanotube reinforced composites. Int. J. Plast. 27, 539–559.

Bobylev, S.V., Mukherjee, A.K., Ovid'ko, I.A., 2009. Emission of partial dislocations from amorphous intergranular boundaries in deformed nanocrystalline ceramics. Scripta Mater. 60, 36–39.

Bobylev, S.V., Mukherjee, A.K., Ovid'ko, I.A., Sheinerman, A.G., 2010. Effects of intergrain sliding on crack growth in nanocrystalline materials. Int. J. Plast. 26, 1629–1644.

Cho, S., Kikuchi, K., Kawasaki, A., 2012. On the role of amorphous intergranular and interfacial layers in the thermal conductivity of a multi-walled carbon nanotube–copper matrix composite. Acta Mater. 60, 726–736.

Ci, L.J., Ryu, Z.Y., Jin-Phillipp, N.Y., Rühle, M., 2006. Investigation of the interfacial reaction between multi-walled carbon nanotubes and aluminum. Acta Mater. 54, 5367–5375.

Clark, B.G., Robertson, I.M., Dougherty, L.M., Ahn, D.C., Sofronis, P., 2005. High-temperature Dislocation-precipitate Interactions in Al Alloys: An in situ Transmission Electron Microscopy Deformation Study. J. Mater. Res. 20, 1792–1801.

Coleman, J., Khan, U., Blau, W., Gunko, Y., 2006. Small but strong: A review of the mechanical properties of carbon nanotube–polymer composites. Carbon 44, 1624–1652.

Dao, M., Lu, L., Asaro, R., Dehosson, J., Ma, E., 2007. Toward a quantitative understanding of mechanical behavior of nanocrystalline metals. Acta Mater. 55, 4041–4065.

Demkowicz, M.J., Argon, A.S., 2005. Liquidlike atomic environments act as plasticity carriers in amorphous silicon. Phys. Rev. B 72, 245205.

Deng, C.F., Wang, D.Z., Zhang, X.X., Li, A.B., 2007. Processing and properties of carbon nanotubes reinforced aluminum composites. Mater. Sci. Eng. A 444, 138–145.

Duan, H.L., Wang, J., Huang, Z.P., Karihaloo, B.L., 2005. Size-dependent effective elastic constants of solids containing nano-inhomogeneities with interface stress. J. Mech. Phys. Solids 53, 1574–1596.

Dundurs, J., Mura, T., 1964. Interaction between an edge dislocation and a circular inclusion. J. Mech. Phys. Solids 12, 177–189.

England, A.H., 1971. Complex Variable Method in Elasticity. John Wiley and Sons, New York.

Esawi, A.M.K., Morsi, K., Sayed, A., Taher, M., Lanka, S., 2010. Effect of carbon nanotube (CNT) content on the mechanical properties of CNT-reinforced aluminium composites. Compos. Sci. Technol. 70, 2237–2241.

Espinosa, H.D., Panico, M., Berbenni, S., Schwarz, K.W., 2006. Discrete dislocation dynamics simulations to interpret plasticity size and surface effects in freestanding FCC thin films. Int. J. Plast. 22, 2091–2117.

Fang, Q.H., Liu, Y.W., 2006. Size-dependent interaction between an edge dislocation and a nanoscale inhomogeneity with interface effects. Acta Mater. 54, 4213–4220.

Fang, Q.H., Li, B., Liu, Y.W., 2007. Interaction between edge dislocations and a circular hole with surface stress. Phys. Stat. Sol. (b) 244, 2576–2588.

Fang, Q.H., Liu, Y.W., Jin, B., Wen, P.H., 2009a. Interaction between a dislocation and a core–shell nanowire with interface effects. Int. J. Solids Struct. 46, 1539–1546.

Fang, Q.H., Liu, Y.W., Jin, B., Wen, P.H., 2009b. Effect of interface stresses on the image force and stability of an edge dislocation inside a nanoscale cylindrical inclusion. Int. J. Solids Struct. 46, 1413–1422.

Fisher, F.T., Bradshaw, R.D., Brinson, L.C., 2003. Fiber waviness in nanotube-reinforced polymer composites—I: Modulus predictions using effective nanotube properties. Compos. Sci. Technol. 63, 1689–1703.

Flahaut, E., Peigney, A., Laurent, C., Marlière, C., Chastel, F., Rousset, A., 2000. Carbon nanotube-metal-oxide nanocomposites: microstructure, electrical conductivity and mechanical properties. Acta Mater. 48, 3803–3812.

Gao, H., 1992. Diffusion or imperfection modified long range interaction between a line dislocation and a spherical inclusion. Int. J. Eng. Sci. 30, 1061–1071.

Gao, S., Mader, E., Plonka, R., 2008. Nanocomposite coatings for healing surface defects of glass fibers and improving interfacial adhesion. Compos. Sci. Technol. 68, 2892–2901.

George, R., Kashyap, K.T., Rahul, R., Yamdagni, S., 2005. Strengthening in carbon nanotube/aluminium (CNT/Al) composites. Scripta Mater. 53, 1159–1163.

Goh, C.S., Wei, J., Lee, L.C., Gupta, M., 2008. Ductility improvement and fatigue studies in Mg-CNT nanocomposites. Compos. Sci. Technol. 68, 1432–1439.

Gurtin, M.E., Murdoch, A.I., 1975. A continuum theory of elastic material surfaces. Arch. Ration. Mech. An. 57, 291–323.

Gutkin, M.Y., Ovidko, I., 2008a. Glide of hollow fibers at the bridging stage of fracture in ceramic nanocomposites. Scripta Mater. 59, 414–417.

Gutkin, M.Y., Ovid'ko, I.A., 2008b. Dislocation mechanism of hollow fiber sliding during ceramic nanocomposite fracture. Phys. Solid State 50, 2053–2061.

Gutkin, M.Y., Enzevaee, C., Shodja, H.M., 2013. Interface effects on elastic behavior of an edge dislocation in a core–shell nanowire embedded to an infinite matrix. Int. J. Solids Struct. 50, 1177–1186.

Hashin, Z., 2002. Thin interphase/imperfect interface in elasticity with application to coated fiber composites. J. Mech. Phys. Solids 50, 2509–2537.

Hill, R., 1964. Theory of mechanical properties of fibre-strengthened materials: I. Elastic behaviour. J. Mech. Phys. Solids 12, 199–212.

Hiratani, M., Zbib, H.M., Khaleel, M.A., 2003. Modeling of thermally activated dislocation glide and plastic flow through local obstacles. Int. J. Plast. 19, 1271–1296.

Hirth, J.P., Lothe, J., 1982. Theory of Dislocations. John Wiley, New York.

Hu, S.Y., Li, Y.L., Zheng, Y.X., Chen, L.Q., 2004. Effect of solutes on dislocation motion — a phase-field simulation. Int. J. Plast. 20, 403–425.

Jia, Y., Peng, K., Gong, X.-L., Zhang, Z., 2011. Creep and recovery of polypropylene/carbon nanotube composites. Int. J. Plast. 27, 1239–1251.

Jiang, L.Y., Huang, Y., Jiang, H., Ravichandran, G., Gao, H., Hwang, K.C., Liu, B., 2006. A cohesive law for carbon nanotube/polymer interfaces based on the van der Waals force. J. Mech. Phys. Solids 54, 2436–2452.

Khraishi, T.A., Yan, L., Shen, Y.-L., 2004. Dynamic simulations of the interaction between dislocations and dilute particle concentrations in metal–matrix composites (MMCs). Int. J. Plast. 20, 1039–1057.

Kim, K., Sudak, L.J., 2005. Interaction between a radial matrix crack and a three-phase circular inclusion with imperfect interface in plane elasticity. Int. J. Fracture 131, 155–172.

Kim, K.T., Cha, S.I., Gemming, T., Eckert, J., Hong, S.H., 2008. The role of interfacial oxygen atoms in the enhanced mechanical properties of carbon-nanotube-reinforced metal matrix nanocomposites. Small 4, 1936–1940.

Kochmann, D.M., Le, K.C., 2008. Dislocation pile-ups in bicrystals within continuum dislocation theory. Int. J. Plast. 24, 2125–2147.

Kumar, K.S., Suresh, S., Chisholm, M.F., Horton, J.A., Wang, P., 2003. Deformation of electrodeposited nanocrystalline nickel. Acta Mater. 51, 387–405.

Kuzumaki, T., Miyazawa, K., Ichinose, H., Ito, K., 1998. Processing of carbon nanotube reinforced aluminum composite. J. Mater. Res. 13, 2445–2449.

Kwon, H., Estili, M., Takagi, K., Miyazaki, T., Kawasaki, A., 2009. Combination of hot extrusion and spark plasma sintering for producing carbon nanotube reinforced aluminum matrix composites. Carbon 47, 570–577.

Li, Q.Q., Viereckl, A., Rottmair, C.A., Singer, R.F., 2009. Improved processing of carbon nanotube/magnesium alloy composites. Compos. Sci. Technol. 69, 1193–1199.

Lim, C.W., Li, Z.R., He, L.H., 2006. Size dependent, non-uniform elastic field inside a nano-scale spherical inclusion due to interface stress. Int. J. Solids Struct. 43, 5055–5065.

Liu, Z.L., Liu, X.M., Zhuang, Z., You, X.C., 2009. A multi-scale computational model of crystal plasticity at submicron-to-nanometer scales. Int. J. Plast. 25, 1436–1455.

Liu, Y.G., Zhou, J.Q., Ling, X., 2010. Impact of grain size distribution on the multiscale mechanical behavior of nanocrystalline materials. Mater. Sci. Eng. A 527, 1719–1729.

Liu, S., Hu, N., Yamamoto, G., Cai, Y.D., Zhang, Y.J., Liu, Y.L., Li, Y., Hashida, T., Fukunaga, H., 2011a. Investigation on CNT/alumina interface properties using molecular mechanics simulations. Carbon 49, 3701–3704.

Liu, Y.G., Zhou, J.Q., Shen, T.D., Hui, D., 2011b. Grain rotation dependent fracture toughness of nanocrystalline materials. Mater. Sci. Eng. A 528, 7684–7687.

Lubarda, V.A., 2011. Emission of dislocations from nanovoids under combined loading. Int. J. Plast. 27, 181–200.

Luo, H.A., Chen, Y., 1991. An edge dislocation in a three-phase composite cylinder model. J. Appl. Mech. 58, 75–86.

Mao, S.X., Li, M.Z., 1999. Effects of dislocation shielding on interface crack initiation and growth in metal/ceramic layered materials. J. Mech. Phys. Solids 47, 2351–2379.

Miller, R.E., Shenoy, V.B., 2000. Size-dependent elastic properties of nanosized structural elements. Nanotechnology 11, 139–147.

Mogilevskaya, S.G., Crouch, S.L., 2004. A Galerkin boundary integral method for multiple circular elastic inclusions with uniform interphase layers. Int. J. Solids Struct. 41, 1285–1311.

Mogilevskaya, S.G., Crouch, S.L., Stolarski, H.K., Benusiglio, A., 2010. Equivalent inhomogeneity method for evaluating the effective elastic properties of unidirectional multi-phase composites with surface/interface effects. Int. J. Solids Struct. 47, 407–418.

Muskhelishvili, N.I., 1953. Some Basic Problems of the Mathematical Theory of Elasticity. Noordhoff, Groningen.

Namilae, S., Chandra, N., 2006. Role of atomic scale interfaces in the compressive behavior of carbon nanotubes in composites. Compos. Sci. Technol. 66, 2030–2038.

Nuriel, S., Liu, L., Barber, A.H., Wagner, H.D., 2005. Direct measurement of multiwall nanotube surface tension. Chem. Phys. Lett. 404, 263–266.

Odegard, G.M., Gates, T.S., Wise, K.E., Park, C., Siochi, E.J., 2003. Constitutive modeling of nanotube–reinforced polymer composites. Compos. Sci. Technol. 63, 1671–1687.

Odegard, G.M., Pipes, R.B., Hubert, P., 2004. Comparison of two models of SWCN polymer composites. Compos. Sci. Technol. 64, 1011–1020.

Ovid'ko, I.A., 2005. Deformation and diffusion modes in nanocrystalline materials. Int. Mater. Rev. 50, 65–82.

Ovid'ko, I.A., Sheinerman, A.G., 2009. Grain size effect on crack blunting in nanocrystalline materials. Scripta Mater. 60, 627–630.

Paliwal, B., Cherkaoui, M., 2012. Estimation of anisotropic elastic properties of nanocomposites using atomistic-continuum interphase model. Int. J. Solids Struct. 49, 2424–2438.

Pavia, F., Curtin, W.A., 2011. Interfacial sliding in carbon nanotube/diamond matrix composites. Acta Mater. 59, 6700–6709.

Qaissaunee, M.T., Santare, M.H., 1995. Edge dislocation interacting with an elliptical inclusion surrounded by an interfacial zone. Quart. J. Mech. Appl. Math. 48, 465–482.

Romanov, A.E., Wagner, T., 2001. On the universal misfit parameter at mismatched interfaces. Scripta Mater. 45, 325–331.

Romanov, A.E., Wagner, T., Ruhle, M., 1998. Coherent to incoherent transition in mismatched interfaces. Scripta Mater. 39, 869–875.

Ru, C.Q., 1999. Three-phase elliptical inclusions with internal uniform hydrostatic stresses. J. Mech. Phys. Solids 47, 259–273.

Rul, S., Lefèvre-schlick, F., Capria, E., Laurent, C., Peigney, A., 2004. Percolation of single-walled carbon nanotubes in ceramic matrix nanocomposites. Acta Mater. 52, 1061–1067.

Schröder, J.H., Arzt, E., 1985. Weak beam studies of dislocation/dispersoid interaction in an ods superalloy. Scripta Met. 19, 1129–1134.

Sharma, P., Ganti, S., Bhate, N., 2003. Effect of surfaces on the size-dependent elastic state of nano-inhomogeneities. Appl. Phys. Lett. 82, 535–537.

Shen, L., Li, J., 2003. Effective elastic moduli of composites reinforced by particle or fiber with an inhomogeneous interphase. Int. J. Solids Struct. 40, 1393–1409.

Shen, L.X., Li, J., 2004. Transversely isotropic elastic properties of single-walled carbon nanotubes. Phys. Rev. B 69, 045414.

Shen, L.X., Li, J., 2005. Transversely isotropic elastic properties of multiwalled carbon nanotubes. Phys. Rev. B 71, 035412.

Shibata, S., Taya, M., Mori, T., Mura, T., 1992. Dislocation punching from spherical inclusions in a metal matrix composite. Acta Metall. Mater. 40, 3141–3148.

So, K.P., Lee, I.H., Duong, D.L., Kim, T.H., Lim, S.C., An, K.H., Lee, Y.H., 2011. Improving the wettability of aluminum on carbon nanotubes. Acta Mater. 59, 3313–3320.

Sudak, L.J., Mioduchowski, A., Alberta., Canada, 2002. A three-phase circular inhomogeneity with imperfect interface under thermomechanical loadings in plane elasticity. Acta. Mech. 158, 43–56.

Szlufarska, I., 2005. A crossover in the mechanical response of nanocrystalline ceramics. Science 309, 911–914.

Tan, H., Jiang, L.Y., Huang, Y., Liu, B., Hwang, K.C., 2007. The effect of van der Waals-based interface cohesive law on carbon nanotube-reinforced composite materials. Compos. Sci. Technol. 67, 2941–2946.

Taya, M., Lulay, K.E., Lloyd, D.J., 1991. Strengthening of a particulate metal matrix composite by quenching. Acta Metall. Mater. 39, 73–87.

Tehrani, M., Safdari, M., Al-Haik, M.S., 2011. Nanocharacterization of creep behavior of multiwall carbon nanotubes/epoxy nanocomposite. Int. J. Plast. 27, 887–901.

Tian, L., Rajapakse, R.K.N.D., 2007. Analytical solution for size-dependent elastic field of a nanoscale circular inhomogeneity. J. Appl. Mech. 74, 568.

Treacy, M.M.J., Ebbesen, T.W., Gibson, J.M., 1996. Exceptionally high Young's modulus observed for individual carbon nanotubes. Nature 381, 678–680.

Walpole, L.J., 1969. On the overall elastic moduli of composite materials. J. Mech. Phys. Solids 17, 235–251.

Walpole, L.J., 1981. Elastic behavior of composite materials: theoretical foundations. Adv. Appl. Mech. 21, 169–242.

Wang, X., Pan, E., 2011. Interaction between an edge dislocation and a circular inclusion with interface slip and diffusion. Acta Mater. 59, 797–804.

Wang, X., Shen, Y.p., 2002. An edge dislocation in a three-phase composite cylinder model with a sliding interface. J. Appl. Mech. 69, 527–538.

Wang, Y., Li, J., Hamza, A.V., Barbee, T.W., 2007. Ductile crystalline-amorphous nanolaminates. Prco. Natl. Acad. Sci. USA 104, 11155–11160.

Wang, Q., Dai, J.F., Li, W.X., Wei, Z.Q., Jiang, J.L., 2008. The effects of CNT alignment on electrical conductivity and mechanical properties of SWNT/epoxy nanocomposites. Compos. Sci. Technol. 68, 1644–1648.

Wang, X., Pan, E., Chung, P.W., 2010. Misfit dislocation dipoles in wire composite solids. Int. J. Plast. 26, 1415–1420.

Wang, L., Zhou, J.Q., Liu, Y.G., Zhang, S., Wang, Y., Xing, W., 2011. Nanovoid growth in nanocrystalline metal by dislocation shear loop emission. Mater. Sci. Eng. A 528, 5428–5434.

Wolf, D., Yamakov, V., Phillpot, S.R., Mukherjee, A., Gleiter, H., 2005. Deformation of nanocrystalline materials by molecular-dynamics simulation: relationship to experiments? Acta Mater. 53, 1–40.

Wu, J., Zhang, Z., Liu, B., Hwang, K.C., Huang, Y., 2009. Numerical analyses for the atomistic-based shell theory of carbon nanotubes. Int. J. Plast. 25, 1879–1887.

Xia, Z., Riester, L., Curtin, W.A., Li, H., Sheldon, B.W., Liang, J., Chang, B., Xu, J.M., 2004. Direct observation of toughening mechanisms in carbon nanotube ceramic matrix composites. Acta Mater. 52, 931–944.

Xiao, Z.M., Chen, B.J., 2001. On the interaction between an edge dislocation and a coated inclusion. Int. J. Solids Struct. 38, 2533–2548.

Xu, C.L., Wei, B.Q., Ma, R.Z., Liang, J., Ma, X.K., Wu, D.H., 1999. Fabrication of aluminum-carbon nanotube composites and their electrical properties. Carbon 37, 855–858.

Yamamoto, G., Omori, M., Hashida, T., Kimura, H., 2008. A novel structure for carbon nanotube reinforced alumina composites with improved mechanical properties. Nanotechnology 19, 315708.

Yang, S., Yu, S., Ryu, J., Cho, J.-M., Kyoung, W., Han, D.-S., Cho, M., 2013. Nonlinear multiscale modeling approach to characterize elastoplastic behavior of CNT/polymer nanocomposites considering the interphase and interfacial imperfection. Int. J. Plast. 41, 124–146.

Yassar, R.S., Mesarovic, S.D., Field, D.P., 2007. Micromechanics of hardening of elastic–plastic crystals with elastic inclusions: I – Dilute concentration. Int. J. Plast. 23, 1901–1917.

Zbib, H.M., Overman, C.T., Akasheh, F., Bahr, D., 2011. Analysis of plastic deformation in nanoscale metallic multilayers with coherent and incoherent interfaces. Int. J. Plast. 27, 1618–1639.

Zhang, W.X., Wang, T.J., Chen, X., 2010. Effect of surface/interface stress on the plastic deformation of nanoporous materials and nanocomposites. Int. J. Plast. 26, 957–975.